

18 Abstract

19 An improved approach to Sp phase common-conversion point stacking that incorporates
20 scattering kernels was applied to the Anatolian region and resolves the boundaries of an
21 asthenospheric low velocity layer. With the new stacking approach, Sp receiver function
22 amplitudes are projected around the converted wave ray paths only to locations with strong
23 sensitivity to horizontal discontinuities. An expression for accurately estimating the standard
24 deviation of the stack amplitude was also derived. This expression is more efficient than
25 bootstrapping and can be used for any problem requiring the standard deviation of a weighted
26 average. We also developed a method to more accurately measure near surface compressional
27 and shear wave velocities, which are used to separate P and SV waveform components by
28 removing free-surface effects. We applied these improved approaches to data from the Anatolian
29 region, using multiple bandpass filters to better image velocity gradients of varying depth
30 extent. Common conversion point stacks of 23,787 Sp receiver functions contain a clear Moho
31 and 410-discontinuity, but also reveal a less common positive velocity gradient at 80-150 km
32 depth beneath most of the region. The latter is particularly prominent at longer periods (10-100
33 s), indicating that it is relatively gradual in depth. This feature represents the base of an
34 asthenospheric low velocity layer that is consistent with high mantle temperatures and the
35 presence of partial melt. At shorter periods (2-20 s), a negative velocity gradient corresponding
36 to the lithosphere-asthenosphere boundary is observed at 60-90 km depth, marking the top of the
37 asthenospheric low velocity layer.

38

39 Plain Language Summary

40 The asthenosphere beneath the Anatolian region is known to have low seismic wave velocities,
41 consistent with mantle that is high temperature and that possibly contains small fractions of
42 partial melt, as suggested by the presence of volcanic fields at the surface. However, the depth of
43 the asthenospheric low velocity layer is not well known. In this study, we locate this low
44 velocity mantle layer by applying a newly developed imaging method to seismic shear waves
45 that convert to compressional waves at the velocity gradients that mark the layer boundaries. The
46 new method more accurately incorporates the physics of seismic scattering into how the wave

47 records are combined to form the images of seismic velocity structure. This study is the first to
48 clearly resolve both the lower and upper margins of the asthenosphere for the whole region. The
49 top of the layer corresponds to the lithosphere-asthenosphere boundary at 60-90 km depth, and
50 this velocity gradient is localized in depth. However, the bottom boundary, which lies at depths
51 of 80-150 km, occurs over a broader depth range and could represent either the onset of melting
52 or a gradual temperature increase with the depth.

53

54 **1. Introduction**

55 Teleseismic body waves that convert from S to P vibration (or vice versa) at velocity or density
56 anomalies are potent tools for imaging velocity discontinuities in the crust and mantle. To
57 isolate the effects of Earth structure, incident phases are often deconvolved from converted
58 phases to remove source and instrument information, resulting in receiver functions (e.g. Farra &
59 Vinnik, 2000) for Ps (incident P wave with converted S wave) and Sp (incident S wave with
60 converted P wave) phases.

61 Common-conversion point (CCP) stacking of receiver functions (e.g. Dueker & Sheehan, 1997)
62 is often used to image mantle discontinuities. During CCP stacking, converted waves are
63 assumed to be generated around converted wave ray paths. Receiver function amplitudes
64 recorded at surface stations are projected back along the paths, and the image is constructed by
65 summing receiver function amplitudes as a function of position, assuming spatial functions that
66 weight how a receiver function on a particular ray path contributes to the summed amplitude at a
67 given location. In prior studies, these spatial functions are either represented by geographic bins
68 of conversion points (e.g. Dueker & Sheehan, 1997; Kind et al., 2012; Rondenay, 2009), or by
69 empirically defined weighting functions that represent Fresnel zones for vertically incident
70 waves (e.g. Lekić & Fischer, 2017; Lekic et al., 2011; Wittlinger & Farra, 2007). However, to
71 incorporate the physics of wave scattering into CCP stacking, these spatial functions should be
72 consistent with the sensitivity kernels that describe how scattering from a point on a velocity
73 discontinuity contributes to an observed converted phase, for example the scattering kernels for
74 Sp and Ps phases (e.g. Bostock & Rondenay, 1999; Bostock et al., 2001; Hansen & Schmandt,
75 2017; Hua et al., 2020; Mancinelli & Fischer, 2017). This condition is typically not met in prior

76 CCP stacking approaches. Therefore, a new CCP stacking scheme is developed here based on
77 the shape of scattering kernels while assuming that velocity structure is laterally invariant
78 (Section 2.2).

79 High quality receiver functions are an essential ingredient of CCP stacking, and accurate incident
80 and converted waveform components are necessary for robust receiver functions. While some
81 studies deconvolve vertical from radial components to represent Ps receiver functions (e.g. Zor et
82 al., 2003), others deconvolve P from SV. However, for Sp receiver functions, deconvolution of
83 SV from P is necessary, due to the more horizontal incidence of Sp phases at the station (e.g.
84 Kind et al., 2012). P and SV components are sometimes approximated using rotation of radial
85 and vertical components into a ray-parallel and ray-normal reference frame (Kind et al., 2012),
86 but, because the recorded seismogram is a combination of incident and reflected waves, other
87 studies calculate P and SV components using the free-surface transform of Kennett (1991) (e.g.
88 Abt et al., 2010; Bostock & Rondenay, 1999). This latter approach is more accurate in isolating
89 incident and converted waveform components, but it requires values for near surface P and S
90 velocities. Building on prior approaches (Abt et al., 2010; Park and Ishii, 2018) this study
91 introduces a new method to accurately measure near surface P and S velocities from P and S
92 particle motions in Section 2.1.

93 Accurate quantification of uncertainties in CCP stack amplitudes are critical to evaluating which
94 features are robust and avoiding over-interpretation. The uncertainty is often quantified by the
95 standard deviation of the stacked receiver function amplitude, for example as measured by
96 bootstrapping (Hopper et al., 2014). During bootstrapping, individual receiver functions are
97 randomly resampled and CCP stacked over multiple iterations, and the standard deviation of
98 amplitude at each point among the multiple CCP stacks is calculated. However, this process is
99 computationally expensive. In this study we derived a theoretical expression for accurately
100 measuring the standard deviation of any weighted average and applied this to CCP stacking
101 (Section 2.3), thus avoiding the need for bootstrapping.

102 With these methodological improvements, Sp receiver function CCP stacking was used to image
103 the upper mantle beneath the Anatolian region (Figure 1). Sp receiver functions were employed
104 because they are not contaminated by crustal reverberations which affect Ps receiver functions in

105 the time window where scattered waves from the shallow upper mantle arrive (Kind et al., 2012;
106 Yuan et al., 2006). In addition, as will be shown in Section 2.2, the sensitivity kernels for Sp
107 receiver functions are more effective at imaging quasi-horizontal upper mantle discontinuities
108 with CCP stacking, particularly for the station spacing available in Anatolia (Figure 1).

109 The Anatolian region lies within the Alpine-Himalayan orogenic belt. In eastern Anatolia,
110 collision between the Arabian and Eurasian plates began in the Oligocene, while central and
111 western Anatolia have been escaping westwards, with their ongoing motion accommodated by
112 the North Anatolian fault zone and the East Anatolian fault zone (e.g. Jolivet et al., 2013;
113 Reilinger et al., 2006; Schildgen et al., 2014; A. M. C. Şengör et al., 2008). Numerous seismic
114 models based on tomography with varied seismic phases have found thin lithosphere and low
115 velocity asthenosphere beneath Anatolia, with particularly low velocities beneath eastern
116 Anatolia; many models also contain dipping high velocity anomalies that have been interpreted
117 as fragments of subducted lithosphere, with zones of lower velocity asthenosphere flowing
118 between them (Bakırcı et al., 2012; Berk Biryol et al., 2011; Blom et al., 2020; Delph et al.,
119 2015; Fichtner et al., 2013; Gans et al., 2009; Govers & Fichtner, 2016; Portner et al., 2018;
120 Salaün et al., 2012; Wei et al., 2019; H. Zhu, 2018). Seismic models are typically consistent with
121 the view that slab detachment occurred earlier beneath eastern Anatolia, creating a broad window
122 filled with hot asthenosphere and surface uplift (Faccenna et al., 2006; Govers & Fichtner, 2016;
123 Keskin, 2003; Schildgen et al., 2014; A. Şengör et al., 2003). Slab fragmentation and
124 asthenospheric influx subsequently propagated west, contributing to uplift in central Anatolia
125 (McNab et al., 2018; Schildgen et al., 2014). The particularly low velocity asthenosphere
126 beneath eastern Anatolia is consistent with elevated mantle potential temperatures inferred from
127 geochemical data (e.g. McNab et al., 2018; Nikogosian et al., 2018; Reid et al., 2017).

128 Constraints on seismic velocity interfaces from converted body waves have also illuminated the
129 properties of the Anatolian crust and mantle. Numerous studies have focused on crustal
130 properties (e.g. Abgarmi et al., 2017; Frederiksen et al., 2015; Karabulut et al., 2019; Licciardi et
131 al., 2018; Ozacar et al., 2008; Vanacore et al., 2013; L. Zhu et al., 2006; Zor et al., 2003).
132 However, two prior studies used Sp phases to image mantle discontinuities. Angus et al. (2006)
133 found Sp phases consistent with a decrease in velocity over the lithosphere-asthenosphere
134 boundary (LAB) at depths of 60-80 km in eastern Anatolia, whereas Kind et al. (2015) inferred

135 LAB velocity gradients at 80-100 km across Anatolia. In this study, we re-visit Sp CCP stacking
 136 in the Anatolian mantle, enhanced by the methodological improvements described above and
 137 additional data, to refine constraints on lithospheric thickness and to search for mantle
 138 discontinuities associated with the base of the asthenosphere.

139

140 2. Methods

141 2.1. Free-surface Velocities and P-SV Phase Separation

142 The Sp receiver functions used in this study rely on accurate calculation of P and SV components
 143 from radial and vertical components based on a free-surface transform (Kennett, 1991) that
 144 removes the effect of free-surface reflection. The transform is expressed as

$$145 \begin{pmatrix} P \\ SV \end{pmatrix} = \mathbf{T}(\alpha^{FS}, \beta^{FS}, p) \begin{pmatrix} R \\ Z \end{pmatrix}, \quad \mathbf{T} = \begin{pmatrix} \frac{p(\beta^{FS})^2}{\alpha^{FS}} & \frac{(\beta^{FS})^2 p^2 - 0.5}{\alpha^{FS} q_\alpha} \\ \frac{0.5 - (\beta^{FS})^2 p^2}{\beta^{FS} q_\beta} & p\beta^{FS} \end{pmatrix}, \quad (1)$$

146 where R and Z are the recorded vertical and the radial components, P and SV are P and SV
 147 components before encountering the free-surface, \mathbf{T} is the free-surface transform matrix, α^{FS}
 148 and β^{FS} are the assumed near-surface compressional velocity (V_p) and shear velocity (V_s), p is
 149 the ray parameter at the station in s/km, and $q_\alpha = [(\alpha^{FS})^{-2} - p^2]^{0.5}$, $q_\beta = [(\beta^{FS})^{-2} - p^2]^{0.5}$.

150 Therefore, accurate estimation of α^{FS} and β^{FS} is required to perform the transform correctly.

151 Previously, Abt et al. (2010) also used equation (1) to obtain P and SV components for receiver
 152 function calculations, and they determined the free-surface velocities by performing a grid search
 153 over α^{FS} and β^{FS} using equation (1) to minimize SV in the P arrival window and P in the S
 154 arrival window. However, this method does not use the information in P for the P arrival, and
 155 information in SV for the S arrival. Other studies have investigated the free surface behavior of
 156 the polarization of the recorded phase (Wiechert & Zoeppritz, 1907) to better constrain α^{FS} and
 157 β^{FS} (Park & Ishii, 2018), and have used the frequency-dependence of the polarization to

158 constrain local velocity stratification (Hannemann et al., 2016; Park et al., 2019; Svenningsen &
 159 Jacobsen, 2007). In this study, a new method is developed for estimating free-surface velocities.
 160 This method incorporates the behavior of P and SV at the free surface, including free surface
 161 reflections, but is not based on direct measurement of polarizations.

162 If the true P and SV components are expressed as P_0 and SV_0 , and the true V_p and V_s are α_0^{FS}
 163 and β_0^{FS} , the recorded R and Z can be expressed as

$$164 \quad \begin{pmatrix} R \\ Z \end{pmatrix} = \mathbf{R}(\alpha^{FS} = \alpha_0^{FS}, \beta^{FS} = \beta_0^{FS}, p) \begin{pmatrix} P_0 \\ SV_0 \end{pmatrix}, \quad \mathbf{R} = \frac{1}{q_\gamma^4 + 4p^2 q_\alpha q_\beta} \begin{pmatrix} \frac{4p\alpha^{FS} q_\alpha q_\beta}{(\beta^{FS})^2} & \frac{2q_\gamma^2 q_\beta}{\beta} \\ -\frac{2\alpha^{FS} q_\gamma^2 q_\alpha}{(\beta^{FS})^2} & \frac{4pq_\alpha q_\beta}{\beta} \end{pmatrix}, \quad (2)$$

165 where $q_\gamma = [(\beta^{FS})^{-2} - 2p^2]^{0.5}$, and \mathbf{R} is the reflection matrix containing reflection coefficients
 166 at the free surface (e.g. Aki & Richards, 2002), which is also the inverse matrix of \mathbf{T} . By
 167 substituting equation (2) into (1), the transformed P and SV components can be expressed as

$$168 \quad \begin{pmatrix} P \\ SV \end{pmatrix} = \mathbf{T}(\alpha^{FS}, \beta^{FS}, p) \mathbf{R}(\alpha_0^{FS}, \beta_0^{FS}, p) \begin{pmatrix} P_0 \\ SV_0 \end{pmatrix}. \quad (3)$$

169 With equation (3), to solve for α_0^{FS} and β_0^{FS} , three particle motion patterns

$$170 \quad \mathbf{C}_1(\alpha^{FS}, \beta^{FS}) = \frac{P \cdot SV}{R \cdot Z}, \quad \mathbf{C}_2(\alpha^{FS}, \beta^{FS}) = \frac{P \cdot P}{R \cdot Z} \quad \text{and} \quad \mathbf{C}_3(\alpha^{FS}, \beta^{FS}) = \frac{SV \cdot SV}{R \cdot Z} \quad (4)$$

171 are first measured for both P and S arrivals (e.g. Figure 2). Specifically, P and SV are
 172 calculated from equation (1) for different α^{FS} (2.7-8.1 km/s with a 0.03 km/s increment) and
 173 β^{FS} (1.5-4.5 km/s with a 0.0167 km/s increment), and the patterns are then calculated using
 174 equation (4), making the observed patterns functions of α^{FS} and β^{FS} . The patterns include
 175 scaling by $R \cdot Z$ to normalize the amplitude of the patterns, so that the amplitude of the
 176 waveform does not affect the results. For the case of a half space with $V_p=4.92$ km/s and $V_s=2.82$
 177 km/s and a P wave with a ray parameter of 0.0482 s/km, the three patterns based on propagator

178 matrix synthetic seismograms (Keith & Crampin, 1977) are shown in Figures 2a to 2c, and the
179 patterns for an SV wave with a ray parameter 0.1098 s/km are shown in Figures 2e to 2g.

180 After obtaining patterns from the observed waveforms, P and SV are then predicted for different
181 α_0^{FS} and β_0^{FS} with equation (3) by setting $SV_0 = 0$ for the P arrival and $P_0 = 0$ for the S arrival,
182 assuming the ray parameter of the real waveform. With the predicted P and SV , the three
183 predicted patterns are calculated according to equation (4) and are labelled as \mathbf{C}_1^P , \mathbf{C}_2^P and \mathbf{C}_3^P .
184 The predicted patterns are not only functions of α^{FS} and β^{FS} but also α_0^{FS} and β_0^{FS} . Optimal
185 α_0^{FS} and β_0^{FS} values are then obtained by matching \mathbf{C}_1^P , \mathbf{C}_2^P and \mathbf{C}_3^P for different α_0^{FS} and β_0^{FS}
186 to \mathbf{C}_1 , \mathbf{C}_2 and \mathbf{C}_3 .

187 In practice, instead of using P and S arrivals together to constrain α_0^{FS} and β_0^{FS} , α_0^{FS} is obtained
188 from S arrival pattern matching, and β_0^{FS} from P arrival pattern matching (Figures 2d & 2h).
189 This choice is motivated by the fact that the P arrival polarization does not depend on α_0^{FS} , a
190 result also shown in Park and Ishii (2018), and therefore the P arrival \mathbf{C}_1 , \mathbf{C}_2 and \mathbf{C}_3 patterns
191 also do not depend on α_0^{FS} . While the value of \mathbf{C}_2 does vary with α^{FS} in the P arrival \mathbf{C}_2
192 pattern (Figure 2b), the \mathbf{C}_2 pattern itself does not vary with values of α_0^{FS} . The independence of
193 the P arrival \mathbf{C}_1 , \mathbf{C}_2 and \mathbf{C}_3 patterns can be demonstrated as follows. From equations (1) and
194 (4), it can be shown that the \mathbf{C}_1 , \mathbf{C}_2 and \mathbf{C}_3 patterns depend only on the polarization R/Z , and
195 from equation (2), the polarization is expressed as

$$196 \quad \frac{R}{Z} = \frac{\mathbf{R}_{11}P_0 + \mathbf{R}_{12}SV_0}{\mathbf{R}_{21}P_0 + \mathbf{R}_{22}SV_0}, \quad (5)$$

197 where the subscripts refer to the row and column of an element in the \mathbf{R} matrix. For the P
198 arrival, $SV_0 = 0$, and the polarization $R/Z = -2pq_\beta/q_\gamma^2$ (equations 2 & 5). Therefore, the
199 polarization is independent of α_0^{FS} . For the S arrival, $P_0 = 0$, and the polarization is equal to
200 $q_\gamma^2/2pq_\alpha$ (equations 2 & 5), which depends on both α_0^{FS} and β_0^{FS} .

201 In practice, using P arrival patterns, a uniform grid search is performed over β_0^{FS} , with 181
 202 values that range from 1.5 km/s to 4.5 km/s, to find the value that minimizes a misfit function
 203 defined as

$$204 \quad \text{misfit} = \sqrt{\|C_1 - C_1^P\|_2^2 + \|C_2 - C_2^P\|_2^2 + \|C_3 - C_3^P\|_2^2}, \quad (6)$$

205 where the L_2 -norm refers to the norm of a vector (i.e. treating C_1 as a vector with 181×181
 206 elements). We then use the β_0^{FS} value from this step together with the S arrival patterns to obtain
 207 α_0^{FS} by minimizing the same misfit function in equation (6), but through a grid search over α_0^{FS}
 208 with a minimum value of 2.7 km/s and a maximum value of 8.1 km/s.

209 This approach differs from that of Park and Ishii (2018) in two significant ways. First, Park and
 210 Ishii (2018) solve for free-surface velocities based on minimizing misfits between observed and
 211 predicted P incidence angles and S polarizations. In contrast, we minimize misfits between
 212 observed and predicted C patterns (equation 6), which are the normalized dot products of P and
 213 SV particle motions (equation 4). Second, Park and Ishii (2018) solve for free-surface P and S
 214 velocities simultaneously, while we first use equation (4) with P arrival data to solve for β_0^{FS}
 215 and then, with fixed β_0^{FS} , use equation (4) with S arrival data to solve for α_0^{FS} . Advantages of
 216 using only the P arrival patterns to solve for β_0^{FS} are that P phases typically have much higher
 217 signal-to-noise ratios than S phases, and trade-offs between α_0^{FS} and β_0^{FS} are to some extent
 218 reduced since P arrival patterns do not depend on α_0^{FS} .

219 The synthetic example in Figure 2 demonstrates the effectiveness of the pattern-matching
 220 method in finding α_0^{FS} and β_0^{FS} . For the grid search over β_0^{FS} using the P arrival, the estimated
 221 value of β_0^{FS} matches the free surface V_s from the model used to generate the synthetics (Figure
 222 2d). In addition, while all the misfit components are minimized at the same value of β_0^{FS} , the C_2
 223 misfit dominates the total misfit relative to C_1 and C_3 . This finding shows the advantage of the
 224 new method over the approach in Abt et al. (2010) which relied only on C_1 . For the S arrival,
 225 the grid search over α_0^{FS} yields a minimum misfit α_0^{FS} that matches V_p in the input model

226 (Figure 2h). However, in this case C_1 , C_2 and C_3 all have substantial contributions to the total
 227 misfit, which again emphasizes the importance of using use all the patterns instead of relying
 228 only on C_1 as in Abt et al. (2010).

229 To obtain free-surface velocities from multiple events at a single station, we first weight the
 230 velocity estimates by a value the describes the quality of the seismic phase, and then take the
 231 weighted mean of estimates for the station. One quality factor is a signal-to-noise ratio measured
 232 with moving signal and noise windows applied to the envelope function of Z for P arrivals, and
 233 to the envelope function of R for S arrivals. Signal-to-noise is defined as the average amplitude
 234 in the 5 s signal window divided by the average amplitude in the 20 s noise window, and the
 235 signal-to-noise of the phase (snr) is defined as the maximum signal-to-noise value within 25 s of
 236 the phase arrival time; phase arrival times were obtained using an array-based method (Lekić &
 237 Fischer, 2014). The second quality factor is the correlation coefficient ($corr$) of the R and Z
 238 components in a 3.5 s window around the phase arrival time. The weighting factor is equal to
 239 the product of these factors if snr is greater than 5 and $corr$ is greater than 0.95. Otherwise the
 240 weighting factor is set to zero and the phase is discarded. After obtaining individual β_0^{FS} values
 241 (equations 4 & 6) and their weights from P arrivals, the station free-surface shear velocity β_s^{FS} is
 242 defined as the weighted mean of the individual values. Assuming β_s^{FS} , individual α_0^{FS}
 243 measurements and their weights are obtained from S arrivals, and the station compressional
 244 velocity α_s^{FS} is calculated using a weighted average. If the number of non-zero weighted P
 245 arrivals is less than four, β_s^{FS} is set to 2.8 km/s, and if the number of non-zero weighted S
 246 arrivals is less than four, α_s^{FS} is set to $1.8\beta_s^{FS}$.

247 To show how the method works well with real data, the free surface velocity determination was
 248 applied to data from station ISP (GE network). The free-surface velocities α_s^{FS} and β_s^{FS} for this
 249 station are the same as the input velocity model used in the synthetic case in Figure 2. Figures
 250 S1a to S1c show the C_1 - C_3 patterns for a P arrival from an earthquake that occurred on 20 July
 251 2014 at $\sim 44.65^\circ\text{N}$, 148.78°E with a ray parameter equal to that of the P arrival in the synthetic
 252 case in Figure 2. The observed patterns are very similar to the synthetic patterns, except for C_3

253 (Figure S1c) where the transformed SV component is not as successfully minimized as in the
 254 synthetic case. The misfit functions from the grid search result are also similar to those from the
 255 synthetic case (Figure 3a versus Figure 2d) with a β_0^{FS} of 2.82 km/s obtained at the minimum
 256 misfit. Values of β_0^{FS} were also obtained for P arrivals from other earthquakes, and their
 257 histogram is shown in Figure 4a. Although different arrivals resulted in different β_0^{FS} values, their
 258 distribution centers around the weighted mean for β_s^{FS} 2.82 km/s nearly symmetrically. The C_1 -
 259 C_3 patterns (Figure S1d to S1f) for an S arrival (from an earthquake that occurred on 18 May
 260 2014 at $\sim 4.25^\circ\text{N}$, 92.76°E with a ray parameter equal to that of the S arrival synthetic case in
 261 Figure 2) are similar to those from the synthetic case with minor differences. The grid search
 262 (Figure 3b) yields misfit functions that are similar to the synthetic case (Figure 2h), with an α_0^{FS}
 263 clearly defined at a value of 4.92 km/s. The distribution of α_0^{FS} values from different S arrivals
 264 shows greater variability than the β_s^{FS} distribution from the P arrivals (Figure 4b versus Figure
 265 4a). This result is partly because the S polarization dependence on α_0^{FS} is weaker than on β_0^{FS}
 266 (Park & Ishii, 2018), and the number of P arrivals with non-zero weights is five times of the
 267 number of S arrivals with non-zero weights since P phases generally have a higher signal-to-
 268 noise ratio. Nonetheless, the α_0^{FS} distribution is still broadly centered around its weighted mean
 269 of 4.92 km/s.

270 After obtaining α_s^{FS} and β_s^{FS} , the P and SV components are calculated with equation (1) by
 271 setting $\alpha^{FS} = \alpha_s^{FS}$ and $\beta^{FS} = \beta_s^{FS}$. The P and SV components for the P and S arrivals employed
 272 in Figure 3 are plotted in Figures 3c and 3d. The SV component is minimal over the P arrival
 273 window, and the P component is minimal over the S arrival window, indicating the success of
 274 the transform with our new approach to finding free-surface velocities.

275

276 2.2. Kernel Based Common-Conversion Point Stacking

277 To better incorporate converted wave scattering into CCP stacking, we have developed spatial
 278 functions that describe how an individual Sp or Ps receiver function contributes to the stack,

279 based on Sp and Ps sensitivity kernels (e.g. Hansen & Schmandt, 2017; Hua et al., 2020;
 280 Mancinelli & Fischer, 2017). During CCP stacking of Sp or Ps receiver functions, phase ray
 281 paths are traced to a given depth and the travel-time of the converted phase from that point to the
 282 station identifies the relevant amplitude from the receiver function. To calculate the stack at a
 283 given horizontal location for that depth, receiver function amplitudes are combined, assuming
 284 amplitude relationships between the location in the stack and the position of ray paths. In prior
 285 studies, these relationships have typically been described as geographic bins (e.g. Dueker &
 286 Sheehan, 1997) or with weighting functions based on vertical path Fresnel zones (e.g. Lekić &
 287 Fischer, 2017; Lekic et al., 2011; Wittlinger & Farra, 2007). Here we develop weighting
 288 functions that more accurately reflect the interaction of Sp and Ps phases with velocity structure
 289 using their sensitivity kernels.

290 The time-dependence of scattering can be illustrated by incident and scattered wave ray paths
 291 (Figure 5). An incident wave travels upward in the radial-vertical plane (r - z plane). The incident
 292 wave encounters a scatterer, a scattered wave is generated and propagates upward to the station,
 293 and it may not travel in the r - z plane. The incident wave travel time from the earthquake location
 294 to the station is defined as τ_i^r , and the incident wave travel time from the earthquake to the
 295 scatterer is defined as τ_i^s . The travel time of the scattered wave from the scatterer to the station
 296 is given as τ_j . The phase delay time between the scattered phase and the incident phase
 297 (equivalent to time in the receiver function) is described as

$$298 \quad T = \tau_i^s + \tau_j - \tau_i^r. \quad (7)$$

299 Scatterers sharing the same T form the phase delay isochron (e.g. Bostock & Rondenay, 1999;
 300 Bostock et al., 2001). Energy from scatterers on the same isochron contributes to receiver
 301 function amplitude at the same time, and the isochrons determine the shape of the scattering
 302 kernels for receiver function amplitudes (e.g. Bostock & Rondenay, 1999; Bostock et al., 2001;
 303 Hansen & Schmandt, 2017; Hua et al., 2020; Mancinelli & Fischer, 2017). This formulation is
 304 based on the Born approximation that scattered waves will not be scattered again, so the travel
 305 time difference can be expressed as equation (7).

306 The shapes of the phase delay isochrons for Sp and Ps phases fundamentally differ. An Sp
307 isochron is illustrated in Figure 6a. This example corresponds to a uniform half space with
308 $V_p=7.8$ km/s and $V_s=4.3$ km/s (typical upper mantle values), an incident S wave ray parameter of
309 0.1098 s/km (same as used in Figures 3 & 4), and a 200 km scattering depth (the depth where the
310 converted wave ray path intersects the isochron). For this case, the Sp isochron corresponds to a
311 delay time of -27.76 s. The isochron is horizontal near its minimum depth at the conversion
312 point (the intersection point with the converted wave ray path), dips more steeply elsewhere, and
313 extends to infinite distance. A Ps isochron is shown in Figure 6b, for an incident P wave ray
314 parameter of 0.0482 s/km (same as used in Figures 3 & 4) and a scattering depth of 200 km.
315 Here the Ps isochron corresponds to a delay time of 21.74 s. The isochron is also horizontal
316 around the conversion point, but this is the maximum depth on the isochron. In addition, the flat
317 portion of the Ps isochron is much smaller than for the Sp isochron, the Ps isochron does not
318 extend to infinite distance, and its slope angle can be as large as 90° .

319 Based on our knowledge of the isochrons, we developed a spatial weighting function for CCP
320 stacking. The weighting function is based on the slope of the isochron, the geometrical distance
321 from the scatterer to the station, and the depth offset between the scattering depth and the
322 isochron. Each of these factors is discussed below.

323 An assumption inherent in CCP stacking is that velocity discontinuities are horizontal over the
324 length scales where amplitudes from different individual converted phases (or receiver functions)
325 are combined. To be consistent with converted phase sensitivity kernels, the amplitude
326 weighting functions that describe these length scales should correspond to the portion of the
327 isochron that is sensitive to horizontal structure, and what controls the sensitivity to discontinuity
328 dip is the slope angle of the isochron (Rondenay et al., 2005). When a discontinuity overlaps
329 with an isochron in space, scatterers on the discontinuity generate scattered waves that are
330 recorded by the station at the same time, and the positive interference of the scattered waves
331 produces a clear phase in the receiver function. Therefore, for CCP stacking, receiver function
332 amplitudes should be projected into the stack along a depth interface only where their isochron
333 slope angle is approximately 0° . This approach differs from migration methods that are designed
334 to image discontinuities with an arbitrary dip angle and in which receiver function amplitude are
335 projected along the whole isochron (e.g. Hua et al., 2020; Zhang & Schmandt, 2019).

336 The isochron slope angle is equal to the angle between the phase delay time gradient (∇T) and
 337 the vertical axis, and can be derived in a similar manner to Hua et al. (2020). From the path
 338 geometry in Figure 5, it can be seen that

$$339 \quad \frac{\partial \tau_i^s}{\partial r} = \frac{\sin \theta_i}{v_i}, \quad \frac{\partial \tau_i^s}{\partial t} = 0, \quad \frac{\partial \tau_i^s}{\partial z} = -\frac{\cos \theta_i}{v_i},$$

$$\frac{\partial \tau_j}{\partial r} = -\frac{\sin \varphi}{v_j}, \quad \frac{\partial \tau_j}{\partial t} = \frac{\sin \phi}{v_j}, \quad \frac{\partial \tau_j}{\partial z} = \frac{\cos \theta_j}{v_j}, \quad (8)$$

340 where v_i is the incident wave velocity, v_j is the scattered wave velocity, θ_i is the angle from
 341 vertical of the incident wave path, θ_j is the scattered wave take-off angle, φ and ϕ are two
 342 angles defined in Figure 5. φ is positive when the scattered wave is traveling in the positive r
 343 direction, and ϕ is positive when the scattered wave is traveling in the negative t direction.

344 Because τ_i^r does not depend on the scatterer location, from equations (7) and (8), the gradient of
 345 T is expressed as

$$346 \quad \nabla T = \left(\frac{\sin \theta_i}{v_i} - \frac{\sin \varphi}{v_j} \right) \mathbf{e}_r + \frac{\sin \phi}{v_j} \mathbf{e}_t + \left(\frac{\cos \theta_j}{v_j} - \frac{\cos \theta_i}{v_i} \right) \mathbf{e}_z \quad (9)$$

347 where \mathbf{e}_r , \mathbf{e}_t and \mathbf{e}_z are unit vector in r , t and z directions. From equation (9), and with some
 348 algebra, the slope angle \mathcal{G} is expressed as

$$349 \quad \mathcal{G} = \arctan \left(\frac{\sqrt{v_i^2 \sin^2 \phi + (v_j \sin \theta_i - v_i \sin \varphi)^2}}{v_j \cos \theta_i - v_i \cos \theta_j} \right). \quad (10)$$

350 To simplify, φ and ϕ are replaced by the dihedral angle between the vertical plane of scattered
 351 wave propagation and the r - z plane (γ) through the geometric relationship

$$352 \quad \sin \phi = \sin \theta_j \sin \gamma, \quad \sin \varphi = \sin \theta_j \cos \gamma, \quad (11)$$

353 where γ is positive when the scattered wave is traveling the positive r direction. By substituting
 354 equation (11) into (10), the slope angle is expressed as

$$355 \quad \mathcal{G} = \arctan \left(\frac{\sqrt{v_i^2 \sin^2 \theta_j + v_j^2 \sin^2 \theta_i - 2v_i v_j \cos \gamma \sin \theta_i \sin \theta_j}}{v_j \cos \theta_i - v_i \cos \theta_j} \right). \quad (12)$$

356 To obtain \mathcal{G} , v_i and v_j are taken from an existing velocity model, and γ is calculated as the
 357 difference between the earthquake back-azimuth and the azimuth from the station to the
 358 scatterer. Because teleseismic events are used, p , the ray parameter, is assumed to be invariant
 359 with horizontal location. Based on Snell's law, the incident wave vertical incidence angle is
 360 expressed as

$$361 \quad \theta_i = \arcsin \left(\frac{v_i R_E p}{R_E - z} \right) \quad (13)$$

362 where R_E represents the earth radius, and z is the depth of the scatterer. To obtain θ_j , at each
 363 station, the 1D velocity structure traversed by the scattered phase is extracted from an existing
 364 velocity model, and 1000 rays whose ray parameters range from 0 s/km to the maximum value
 365 (i.e. the ray parameter for a horizontal wave at the surface) with a uniform increment are shot
 366 from the station. All points along each of the 1000 paths are labeled with their corresponding ray
 367 parameter, and scattered wave ray parameters for all locations in space can then be retrieved by
 368 interpolating the ray parameter relationship. θ_j is obtained by substituting the scattered wave ray
 369 parameter and v_j into equation (13).

370 To help visualize isochron slope angles, slope angle values from equation (12) are color-coded
 371 on the isochrons in Figure 6. The near-horizontal region is much larger on the Sp isochron than
 372 on the Ps case, even though the isochrons are sampling a horizontal discontinuity at the same
 373 depth. In contrast, the Ps isochrons have larger regions with steeper dips including significant
 374 near-vertical portions, explaining the ability of Ps receiver functions to image vertical
 375 discontinuities (e.g. Hansen & Schmandt, 2017). The slope angle distribution of points at 200 km

376 depth for the Sp case in Figure 6a is shown in Figure 7a. The slope angle is minimized around
 377 the conversion point in a zone that is elongated in the r direction and symmetric about the r axis.

378 While isochrons control the overall shape of the scattering kernel, their overall amplitude is
 379 scaled by geometric spreading of the scattered wave from the scatterer to the station, and
 380 geometric spreading is to the first order inversely proportional to the geometric distance from the
 381 station to the scatterer (Hansen & Schmandt, 2017). Geometric distance from points at 200 km
 382 depth for the case in Figure 6 is shown in Figure 7b, where the smallest values lie below the
 383 station. During CCP stacking of Sp phases, although some points far from the station may have a
 384 relatively flat isochron, the receiver function amplitude should not make a significant
 385 contribution there because of the small geometric spreading value.

386 A third consideration is that receiver function amplitudes for a given converted wave ray path
 387 should not be projected to locations in the CCP stack where the depth offset between the
 388 isochron and the conversion point (e.g. the offset between the isochron and 200 km depth in
 389 Figure 6) is large. To estimate the depth offset at different locations, the slope angles of the
 390 isochron along the r axis (\mathcal{G}_r) and t axis (\mathcal{G}_t) are calculated based on the direction of ∇T in
 391 equation (9), and are expressed as

$$392 \quad \mathcal{G}_r = \arctan\left(\frac{v_i \sin \theta_j \cos \gamma - v_j \sin \theta_i}{v_j \cos \theta_i - v_i \cos \theta_j}\right), \quad \mathcal{G}_t = \arctan\left(-\frac{v_i \sin \theta_j \sin \gamma}{v_j \cos \theta_i - v_i \cos \theta_j}\right). \quad (14)$$

393 The depth offset (Δz) is then estimated to the first order as

$$394 \quad \Delta z = \tan \mathcal{G}_r \Delta r + \tan \mathcal{G}_t \Delta t \quad (15)$$

395 where Δr and Δt are the horizontal offsets from the imaging location to the conversion point in
 396 the r and t directions. For the case in Figure 6a, the true depth offset that is directly measured by
 397 calculating the depth difference between the isochron and 200 km depth is shown in Figure 7c,
 398 and the Δz estimate based on equation (15) is shown in Figure 7d. The first order values from
 399 equation (15) reflect the true depth offset reasonably well closer to the conversion point, but at
 400 more distant locations, equation (15) tends to overestimate the depth offset. However, because

401 receiver function amplitudes should be projected to locations where the depth offset is small,
 402 such overestimation helps to make our stacking method more conservative.

403 A weighting function, W_1 , was designed to limit the projection of receiver function amplitudes to
 404 stack locations with relatively flat isochrons, smaller distances to the station and smaller depth
 405 offset to the isochron.

$$406 \quad W_1 = \frac{z}{d} \exp\left(-\frac{\mathcal{G}^2}{2\sigma_{\mathcal{G}}^2}\right) \exp\left(-\frac{\Delta z^2}{2\sigma_z^2}\right), \quad (16)$$

407 where z is the depth of the imaging point in the stack, and d is the geometrical distance from
 408 the station to the imaging point. $\sigma_{\mathcal{G}}$ is a slope angle threshold, and at points with \mathcal{G} larger than
 409 $\sigma_{\mathcal{G}}$ amplitudes are down-weighted. σ_z depth offset threshold, with a similar function relative to
 410 Δz . In practice $\sigma_{\mathcal{G}}$ is chosen to be 5° , and σ_z is calculated by

$$411 \quad \sigma_z = T_{RF} \frac{dz}{dT_j}, \quad (17)$$

412 where T_{RF} is the half-width of the Gaussian that is convolved with the receiver function during
 413 time-domain deconvolution (Ligorria & Ammon, 1999) to smooth the receiver function. T_j is
 414 the phase delay time (defined in the same way as T) along the converted wave ray path, while
 415 dz/dT_j is the inverse of its vertical derivative. Therefore, σ_z characterizes the vertical imaging
 416 uncertainty that is introduced during receiver function generation.

417 Weighting functions are distorted ellipses that have their maxima at the conversion point and are
 418 elongated in the r direction. The Sp weighting function for the case in Figure 6a is illustrated in
 419 Figure 7e, while the weighting function for the Ps example is shown in Figure 7f. For mantle
 420 discontinuities at the same depth, the Ps weighting function occupies a much smaller area,
 421 indicating that CCP stacking without artificial interpolation or smoothing requires denser station
 422 spacing for Ps phases than for Sp. Because of the broader lateral extent of their weighting
 423 functions, CCP stacking of Sp phases is better suited to imaging near-horizontal discontinuities

424 with stations spaced at more than 20-30 km. In addition, CCP stacking of Sp phases avoids
 425 artifacts related to crustal reverberations that are often strong features in Ps CCP images.

426 To calculate the CCP stack in practice, W_1 is set to zero where its value is less than 0.02 or the
 427 horizontal angular distance to the station is more than 10° . To weight all receiver functions
 428 equally, a normalized weighting function, W_2 , is calculated as:

$$429 \quad W_2 = \frac{W_1}{\sum_{horizontal} W_1}. \quad (18)$$

430 W_2 is simply W_1 divided by the sum of all W_1 at the same depth, so it would add up to one at
 431 each depth, and thus different receiver functions are weighted identically. At each imaging point,
 432 the CCP stacked receiver function amplitude (RF_s) can be expressed as

$$433 \quad RF_s = \frac{\sum_k (W_2)_k RF_k}{\sum_k (W_2)_k}, \quad (19)$$

434 which is the weighted average of individual receiver function amplitudes (RF_k) from different
 435 records, and the subscript k refers to the index of the individual record.

436

437 2.3. The Standard Deviation of a Weighted Average

438 In order to interpret a CCP stack, knowledge of the uncertainties in the stack amplitude are
 439 necessary to assess which structural features have amplitudes that exceed the uncertainty
 440 threshold. In some previous studies, the stack amplitude uncertainty was estimated by
 441 bootstrapping the CCP stacking process (e.g. Hua et al., 2018). The CCP stack was constructed
 442 multiple times based on random samples of the receiver functions, and these individual stacks
 443 were represented by their bootstrap mean at each point, with the bootstrap standard deviation at
 444 each point indicating the uncertainty. However, receiver functions often number in the tens of
 445 thousands, with thousands of receiver functions contributing to each image point. This volume
 446 of data requires a very large number of CCP stack iterations to get a reliable standard deviation

447 from bootstrapping, resulting in a high computational cost. Therefore, we have developed a new
 448 approach to measuring the standard deviation of a weighted average. In particular, this approach
 449 is appropriate for cases where the sums of the weights are allowed to vary while the weights
 450 themselves could be dependent on the sample.

451 For a weighted average in the same form as equation (19), when the number of samples (n) is
 452 large enough, the central limit theorem indicates that the weighted average of a random sample
 453 can be expressed as

$$454 \quad \frac{\sum wx}{\sum w} = \frac{\frac{1}{n} \sum wx}{\frac{1}{n} \sum w} \cong \frac{\mu_{wx} + \frac{1}{\sqrt{n}} \sigma_{wx} \varepsilon_1}{\mu_w + \frac{1}{\sqrt{n}} \sigma_w \varepsilon_2}, \quad (20)$$

455 where w is the weight and x is the sample value, μ_{wx} and μ_w stand for expected values of wx
 456 and w , σ_{wx} and σ_w are standard deviations for wx and w , and both ε_1 and ε_2 follow the
 457 normal distribution $N(0,1)$. For equation (20) to be valid, samples are required to be
 458 independent and with the same distribution, and the same is true for the weights. However, the
 459 weights do not necessarily need to be independent of the samples. When n is large enough,
 460 equation (20) can be approximated by a Taylor expansion as

$$461 \quad \frac{\mu_{wx} + \frac{1}{\sqrt{n}} \sigma_{wx} \varepsilon_1}{\mu_w + \frac{1}{\sqrt{n}} \sigma_w \varepsilon_2} = \frac{1}{\mu_w} \left(\mu_{wx} + \frac{1}{\sqrt{n}} \sigma_{wx} \varepsilon_1 \right) \left[1 - \frac{1}{\sqrt{n} \mu_w} \sigma_w \varepsilon_2 + O\left(\frac{1}{n}\right) \right], \quad (21)$$

$$= \frac{1}{\mu_w} \left[\mu_{wx} - \frac{\mu_{wx}}{\sqrt{n} \mu_w} \sigma_w \varepsilon_2 + \frac{1}{\sqrt{n}} \sigma_{wx} \varepsilon_1 + O\left(\frac{1}{n}\right) \right]$$

462 The first term in the bracket characterizes the expectation of the average, while the other two
 463 terms characterize the variability of the weighted average. Therefore, the expectation (E) and the
 464 variance (V) of the weighted average are expressed as

$$\begin{aligned}
E\left(\frac{\sum wx}{\sum w}\right) &= \frac{\mu_{wx}}{\mu_w} \\
V\left(\frac{\sum wx}{\sum w}\right) &= \frac{1}{n\mu_w^2} V\left(\sigma_{wx}\varepsilon_1 - \frac{\mu_{wx}}{\mu_w}\sigma_w\varepsilon_2\right) \\
&= \frac{1}{n\mu_w^2} \left[\sigma_{wx}^2 + \frac{\mu_{wx}^2}{\mu_w^2}\sigma_w^2 - \frac{2\mu_{wx}}{\mu_w}\sigma_{wx}\sigma_w\rho(\varepsilon_1, \varepsilon_2) \right]
\end{aligned} \tag{22}$$

where ρ stands for the correlation. The correlation can be expressed as

$$\rho(\varepsilon_1, \varepsilon_2) = \rho(\sum wx, \sum w) = \frac{Cov(\sum wx, \sum w)}{\sqrt{V(\sum wx)V(\sum w)}} \tag{23}$$

based on the central limit theorem (equation 20), where Cov stands for covariance. The sample covariance $Cov(\sum wx, \sum w)$ is equal to n times the population covariance $Cov(wx, w)$, since Cov is a bilinear operator and samples are independent. The correlation in equation (23) can be further derived as

$$\rho(\varepsilon_1, \varepsilon_2) = \frac{nCov(wx, w)}{\sqrt{n^2V(wx)V(w)}} = \frac{Cov(wx, w)}{\sigma_{wx}\sigma_w} \tag{24}$$

In practice, μ_{wx} , μ_w , σ_{wx} , σ_w and $Cov(wx, w)$ can be estimated from samples as

$$\mu_{wx} = \overline{wx}, \quad \mu_w = \overline{w}, \quad \sigma_{wx} = \sqrt{\overline{w^2x^2} - \overline{wx}^2}, \quad \sigma_w = \sqrt{\overline{w^2} - \overline{w}^2}, \quad Cov(wx, w) = \overline{w^2x} - \overline{wx}\overline{w}, \tag{25}$$

where the bar indicates the sample average. By substituting equations (24) and (25) into equation (22), and after some algebra, the standard deviation (Std) of the weighted average, which is the square root of the variance in equation (22), can be expressed as

$$Std\left(\frac{\sum wx}{\sum w}\right) = \frac{\sqrt{(\sum w^2x^2)(\sum w)^2 + (\sum w^2)(\sum wx)^2 - 2(\sum w)(\sum wx)(\sum w^2x)}}{(\sum w)^2} \tag{26}$$

479 In the case of CCP stacking, where x is receiver function amplitude and w is W_2 , equation (26)
480 characterizes the uncertainty of stack amplitude at each point in the stack volume. However, this
481 expression can also be applied to any weighted mean where samples are independent but drawn
482 from the same distribution, and weights are independent but drawn from the same distribution.

483 To show the effectiveness of the standard deviation expression in equation (26), a numerical
484 experiment was designed. We randomly generated 648 samples based on a normal distribution
485 $N(0.02, 0.08^2)$, and the corresponding weights were randomly generated based on a normal
486 distribution $N(0.7, 0.4^2)$. The histograms of the resulting samples and weights are shown in
487 Figures 8a and 8b, and the standard deviation of the weighted mean of these data from equation
488 (26) is shown by the black line in Figure 8c. For comparison, 50,000 iterations of bootstrapping
489 were also performed on these data. In each iteration, 648 random values were drawn from the
490 samples and weights, and their weighted average was calculated. After each iteration, the
491 estimated standard deviation of the weighted averages based on the last and all previous
492 iterations was calculated. For this case, the bootstrapped standard deviation starts to converge to
493 a stable value after $\sim 1,000$ iterations, and the value it converges to is very close to the weighted
494 standard deviation from equation (26) which is based on only one calculation. To show how
495 these standard deviation estimates compare to the true standard deviation, a Monte Carlo
496 simulation was designed. Instead of using one set of sample and weights (Figures 8a & 8b) as in
497 the bootstrap case, at every iteration, a new set of sample and weights was generated based on
498 the true distribution, and the weighted average was calculated. Then, the standard deviation
499 calculated from the last on all previous sets of sample and weights was stored. The weighted
500 standard deviation from the Monte Carlo simulation converges to a value which should
501 approximate the true standard deviation (Figure 8c). This value is close to the equation (26)
502 weighted standard deviation, but is offset by a small amount, because the single set of samples
503 and weights used in equation (26) does not strictly follow the overall distributions. However, the
504 good agreement between the estimate from equation (26) and both the true and bootstrap
505 standard deviations demonstrates the accuracy of the much more efficient equation (26)
506 approach.

507 We also compared the weighted standard deviation from equation (26) to the bootstrap standard
508 deviation from the receiver function data in the real CCP stack (Figure 8d). In this example, for
509 an imaging point located at 40.5°N, 38°E and 125 km depth, there are 648 individual receiver
510 functions that have non-zero W_2 (equation 18). However, because in practice bootstrapping of
511 the CCP stack would be performed over all 23,787 receiver functions, the sample size in this
512 example is 23,787, although only 648 samples have non-zero weights. Again the weighted
513 standard deviation from equation (26) equals the value to which the bootstrapping converges,
514 although in this case reasonable convergence requires ~600 iterations.

515 Therefore, the approach summarized in equation (26) is an accurate and computationally fast
516 means of calculating the standard deviation of a weighted average, and is applicable to CCP
517 stacking, but also to a wider range of problems. This approach is especially suitable for
518 problems where the sum of the weights is not fixed, since a much simpler expression can be used
519 when the sum is fixed. For example, equation (26) can also be used to quantify the standard
520 deviation of the measured free-surface velocity in Section 2.1. In addition, equation (26) is also
521 powerful in the sense that it does not require the weight to be independent of the sample value,
522 since the correlation between the weighted sum and the sum of the weights (equation 24) is
523 considered in the derivation.

524

525 **3. Data Processing**

526 Data used in this study are Sp phases from broadband seismograms recorded from as early as
527 1990 to 2019 by 453 seismic stations around the Anatolian region (Figure 1) available from the
528 International Federation of Digital Seismograph Networks (FDSN). Among all the stations, 153
529 of them are permanent stations from the network KO (Kandilli Observatory and Earthquake
530 Research Institute Bosphorus Univ., 2001). Other contributing stations consist of 58 permanent
531 stations from 10 networks (GE, HL, TU, CQ, HT, GO, HC, MN, IU, AB) and 242 temporary
532 stations from 14 networks (YB, YL, YI, XW, XY, Z3, ZZ, XO, XH, YF, TK, SU, SD). Network
533 references appear in the Acknowledgements.

534 Seismic records were retrieved for earthquakes with epicentral distances between 30° and 90°
535 and a minimum moment magnitude of 5.8. To determine appropriate phase windows for P and S
536 arrivals, the arrival time of the phases was picked using an array-based method (Lekić & Fischer,
537 2014) that results in more robust phase identification than from individual records. The
538 seismograms were then filtered by a 4-100 s bandpass filter, and the free-surface velocities are
539 calculated based on the method described in section 2.1. In addition, 2-20 s and 10-100 s
540 bandpass filters were also used to help better detect different velocity structures, and will be
541 discussed in section 4. After retrieving the free-surface velocities, the P and SV components of
542 the seismic records were calculated from equation (1). The signal-to-noise ratios of the S phases
543 were then measured from the SV component, using the ratio of the mean amplitude in a 5 s
544 signal window to the mean amplitude in a 25 s noise window.

545 Sp receiver functions were then obtained by deconvolving the SV component of the direct S
546 arrival from the P component which contains the Sp precursors. Deconvolution was performed
547 using a time-domain deconvolution method (Ligorria & Ammon, 1999). The resulting impulse
548 responses were convolved with a Gaussian whose half-width is 1 s and whose peak value is 1.
549 However, while P and S phases from all distances were used for measuring the free-surface
550 velocity, only earthquakes with epicentral distances between 55° and 85° were used to generate
551 Sp receiver functions. With these criteria, 66,693 Sp receiver functions were generated. We
552 then eliminated receiver functions with a signal-to-noise ratios of less than two, or for which the
553 difference between the arrival time determined from the array-based method and the prediction
554 of the AK135 reference model (Kennett et al., 1995) is more than 10 s.

555 To migrate the receiver functions to depth, we used 1D velocity models that reflect velocity
556 along the converted P phase ray path from the recent full-waveform inversion model (Blom et
557 al., 2020). Using a model derived from full-waveform inversion is advantageous because
558 absolute velocities are inverted for directly, and because this method is especially well suited for
559 areas with significant heterogeneity such as Anatolia. For stations outside the limits of the
560 velocity model, the velocity at the closest location was used. Instead of directly using V_p from
561 Blom et al. (2020), we calculated the average V_p / V_s at every depth in the study region (33° -
562 45° N and 23° - 48° E) and used the average V_p / V_s multiplied by V_s to obtain V_p . V_s is better-
563 resolved than V_p in the model of Blom et al. (2020) for two reasons. First, because V_s is always

564 lower than V_p , sensitivity kernels for this parameter are more spatially constrained than those for
 565 V_p and thus contain more detail. Second, full-waveform inversion models are dominated by
 566 surface waves, which naturally have stronger sensitivity to V_s . Our approach avoids zones with
 567 unrealistic V_p/V_s values due to this heterogeneous sensitivity. The V_s model used in this paper
 568 for migration is the shear velocity model corresponding to SV particle motion.

569 A range of criteria were applied to the migrated receiver functions to eliminate outliers. A
 570 prominent Moho is evident across the study region both in this study and in prior work (e.g.
 571 Abgarmi et al., 2017; Frederiksen et al., 2015; Karabulut et al., 2019; Licciardi et al., 2018;
 572 Ozacar et al., 2008; Vanacore et al., 2013; L. Zhu et al., 2006; Zor et al., 2003). Since the Moho
 573 predicts strong negative phases in Sp receiver functions, we discarded receiver functions without
 574 such signals at shallow depths. Receiver function negative amplitudes in the range from 15 km to
 575 60 km depth were used to form a vector \mathbf{rf}_{sn} , and receiver functions with $\|\mathbf{rf}_{sn}\|_2^2$ smaller than
 576 20% of the median $\|\mathbf{rf}_{sn}\|_2^2$ from all receiver functions were discarded. In addition, using positive
 577 amplitudes between 15 km and 60 km depth form the vector \mathbf{rf}_{sp} , receiver functions with $\|\mathbf{rf}_{sp}\|_2^2$
 578 greater than 3 times the median $\|\mathbf{rf}_{sp}\|_2^2$ from all receiver functions were discarded. In addition,
 579 receiver functions with large and physically non-plausible amplitude variations were also
 580 eliminated. Receiver function amplitudes predicted by the Blom et al. (2020) model provide a
 581 reasonable benchmark for plausible receiver function amplitudes. For the minimum, median
 582 and maximum S wave ray parameters of all seismic records, synthetic seismograms were
 583 calculated for V_s as a function of depth from Blom et al. (2020) at 1° horizontal increments,
 584 using the propagator matrix method (Keith & Crampin, 1977). Receiver functions were
 585 generated from the synthetic waveforms using the same approach that was applied to the data.
 586 From the synthetic receiver functions for the entire study region, the minimum (\mathbf{rf}_{min}) and
 587 maximum (\mathbf{rf}_{max}) amplitudes were found, together with their mean value (\mathbf{rf}_{mean}). The half-
 588 width of the amplitude range \mathbf{rf}_{hw} was defined as $(\mathbf{rf}_{max} - \mathbf{rf}_{min})/2$. To eliminate observed
 589 receiver functions (\mathbf{rf}) with abnormally large amplitudes, receiver functions with $\|\mathbf{rf} - \mathbf{rf}_{mean}\|_2^2$
 590 greater than five times the median $\|\mathbf{rf} - \mathbf{rf}_{mean}\|_2^2$ from all receiver functions were discarded. In

591 addition, to remove sustained large amplitudes in the mantle which are not indicated by the
 592 Blom et al. (2020) model, depth layers greater than 60 km where the receiver function amplitude
 593 \mathbf{rf} is either smaller than $\mathbf{rf}_{mean} - 0.8\mathbf{rf}_{hw}$ or larger than $\mathbf{rf}_{mean} + 0.8\mathbf{rf}_{hw}$ were counted, with their
 594 number indicated as n_d . We then discarded all receiver functions with n_d larger than the median
 595 of n_d from all receiver functions. The n_d criterion is the strictest test we applied, as it removes
 596 half of the data, and it significantly reduces noise in the mantle depth range.

597 CCP stacking was applied to the remaining 23,787 receiver functions (as described in Section
 598 2.2), and the stack uncertainties were calculated (Section 2.3). The conversion points at 125 km
 599 depth (Figure 9) illustrate that much of the Anatolian region is sampled by the measurements. At
 600 each node in a grid with 0.1° spacing horizontally and 0.5 km spacing in depth, the migrated
 601 receiver functions were stacked based on equation (19), and the standard deviation of the stacked
 602 result was estimated by equation (26). To quantify the amount of receiver function information at
 603 each point in the stack, the weights for individual receiver functions at the same node were
 604 summed $\sum W_2$ (equation 18) to obtain a value called W_s . Only features with relatively large W_s
 605 were interpreted, partly to ensure sufficient data were used for the stacking at the place, and
 606 partly because the standard deviation formulation (equation 26) is only valid when the number of
 607 samples is large enough. However, because receiver functions were not projected to depths
 608 where the ray parameter is larger than the critical ray parameter of the P wave, the horizontal
 609 sum of W_s at greater depths is always smaller than the sum at smaller depths. Therefore, in order
 610 to eliminate bias due to this effect, W_s is normalized to a new depth-insensitive weighting W_3 as

$$611 \quad W_3 = \frac{W_s}{\sum_{horizontal} W_s} \cdot \frac{\left(\sum_{vertical} \sum_{horizontal} W_s \right)}{n_{layer}}, \quad (27)$$

612 where n_{layer} is the number of depth layers (901 in this study). CCP stacking results were only
 613 interpreted at points with W_3 over 0.4. The W_3 distribution of the region at 125 km depth is
 614 shown in Figure 9, and for most of the continental Anatolian region W_3 exceeds the 0.4 threshold

615 for interpretation. In addition, the CCP stack is interpreted only if the standard deviation is less
616 than 0.01 or less than half of the weighted and stacked receiver function amplitude.

617 As an example, the CCP stack on profile A-A', which crosses the Anatolian region from east to
618 west (Figure 10a), indicates a Moho that is partially imaged (red phase at 30-50 km depth), a
619 410-discontinuity that extends across most of the profile, and a negative velocity gradient at
620 depths of 360-370 km that has been observed elsewhere and interpreted as the top of a low
621 velocity layer just above the 410-discontinuity (e.g. Vinnik & Farra, 2002). We also observe a
622 prominent mantle arrival at depths of 80-150 km, indicative of a velocity increase with depth,
623 that will be discussed further below. A weak positive velocity gradient is also observed around
624 250 – 300 km depth in some locations. Figure 10b shows that the standard deviation of the
625 profile is typically small and uniform below 100 km depth. However, the standard deviation
626 above 50 km is much larger, even at points with large W_3 (Figure 10c), and cannot be interpreted
627 except at points where the Moho Sp phase has a large enough amplitude to exceed twice of the
628 large standard deviation. Unlike the standard deviation, the W_3 weight distribution is highest
629 along groups of dense converted P ray paths and is larger overall above 300 km depth (Figure
630 10c).

631

632 **4. Results and Discussion**

633 To show how the kernel based CCP stacking method introduced in section 2.2, the free-surface
634 velocity determination method introduced in section 2.1, and the chosen velocity model
635 influence the CCP stacking results, we calculated the CCP stack for three additional cases. In the
636 first, we used the same collection of receiver functions, but with the stacking method in Hua et
637 al. (2018), which employed an empirical weighting function defined by a vertical ray Fresnel
638 zone similar to that in Lekić and Fischer (2017) assuming a dominant frequency of 13 s. The
639 result for cross-section A-A' appears in Figure 11a, but because the weighting function here is
640 defined differently from the weighting function in section 2.1, the image is shown where W_3 is
641 more than 40 instead of 0.4. While the same major phases (Moho, 410 discontinuity, negative
642 amplitudes at 80-150 km) appear in both cases, in the kernel based CCP stacking (Figure 10a)

643 they are more continuous, and the rest of the image contains less small-scale variation in
644 amplitude. This improvement is likely the result of the more physically correct weighting
645 function in the kernel-based stack that individually determines the sensitivity to horizontal
646 discontinuities for each individual receiver function and enables them to more correctly interfere
647 at the appropriate location.

648 We also tested the improvement in the clarity of the CCP stack from the new approach to
649 determining free-surface velocities. In this case (Figure 11b) we use the same set of receiver
650 functions and the older stacking method used in Figure 11a, but with the free surface velocity
651 determination method used in Hopper et al. (2014) which is essentially that of Abt et al. (2010).
652 The differences between the two cases are subtle, but the more accurately determined free
653 surface velocities use in Figure 11a result in slightly different amplitudes for the negative phase
654 at 80-150 km depth. This comparison suggests that the new approach provides only an
655 incremental improvement. Nonetheless, more accurately constrained free surface velocities
656 contribute confidence to the CCP stack, and in addition they are a valuable tool for studying near
657 surface structures (e.g. Park & Ishii, 2018; Park et al., 2019). In addition, this test also indicates
658 that even if free-surface velocities are not estimated very precisely, their influence on mantle
659 CCP stacking is likely not large as long as the values are reasonably accurate.

660 To verify that the velocity model we chose (Blom et al., 2020) to migrate the receiver functions
661 and calculate the CCP stack does not overly influence the CCP stack results, we also employed
662 the kernel based CCP stacking with the velocity model for Anatolia from Fichtner et al. (2013).
663 However, in this case we directly used both V_p and V_s given by the model. The results of this
664 case (Figure 11c) are similar to those obtained when using Blom et al. (2020) (Figure 10a).
665 Noticeable differences are that the negative phase at 80 – 150 km depth is slightly stronger at
666 $\sim 36^\circ\text{E}$ when using Fichtner et al. (2013), but more continuous at 38°E - 39°E with Blom et al.
667 (2020), and the 410 discontinuity is in general more continuous with Blom et al. (2020), while a
668 shallower 410 discontinuity is evident at 33 - 39°E when using Fichtner et al. (2013). However,
669 these differences are relatively minor, and the overall agreement indicates that the CCP stack
670 structures are not dramatically influenced by the assumed velocity model.

671 The negative Sp phase at depths of 80 – 150 km persists widely beneath Anatolia, regardless of
672 the stacking method and migration velocity model. Unlike the Moho and 410 discontinuity,
673 which are expected globally, the negative upper mantle discontinuity is a more unusual feature.
674 This negative Sp phase, which corresponds to a shear velocity increase with depth, is broadly
675 consistent with V_s gradients in the model of Blom et al. (2020). The depth of the Sp phase
676 (Figure 10a) lies near the base of a layer that is dominated by low velocities in the Blom et al.
677 (2019) model (Figure 12a). The calculated vertical V_s gradients Blom et al. (2020) (Figure 12b)
678 agree with the overall position of the negative Sp phase at longitudes of 31°E to 41°E, and from
679 41°E to 44°E, where the CCP stack only shows only weak negative Sp energy that is distributed
680 over a broad range of depths (Figure 10a), vertically-localized positive velocity gradients are also
681 not clearly observed in the velocity model (Figure 12b). However, some features disagree. For
682 example, the positive velocity gradient at 200 km depth from 30°E to 32°E in the Blom et al.
683 (2020) model is not matched clearly by a feature in the CCP stack. Comparison of the CCP stack
684 with V_s and the vertical V_s gradient from Fichtner et al. (2013) (Figures S2a and S2b) show a
685 similar level of agreement. All shear velocity profiles from full-waveform tomography models in
686 this study (Figures 12, S2 & S3) correspond to SV velocity.

687 The widespread presence of the negative Sp phase at depths of 80 – 150 km is demonstrated by
688 other cross-sections through the CCP stack. Cross-section B-B' (Figure 13a) which is south of
689 A-A' also contains the negative Sp phase at 80 – 150 km depth from 29°E to 40°E, as well as
690 from 42°E to 44°E beneath eastern Anatolia. The phase is also observed in north-south striking
691 cross-sections (Figure 14), and it extends from 38°N to 40.5°N in the west (Figure 14a), from at
692 least 37°N to 41°N in central-eastern Anatolia (Figure 14b), and from 37.5°N to 41.5°N in part
693 of easternmost Anatolia (Figure 14c). However, the phase is not strong ubiquitously. Its
694 amplitude and continuity are strongly diminished in much of the region north of 41°N-41.5°N, as
695 shown in Figures 14a and 14b, and in the east-west cross-section C-C' (Figure 13c). This
696 decrease in the amplitude of the negative Sp phase north of the plate boundary broadly correlates
697 with a reduction of the intensity of the low velocity layer whose base it marks, as shown by a
698 comparison of the Blom et al. (2019) shear velocity model on profiles B-B' (Figure S3a) and A-
699 A' (Figure 12) versus C-C' (Figure S3b). A similar trend appears in the shear velocity models of
700 Fichtner et al. (2013), and a third full-waveform inversion that spans Anatolia (H. Zhu, 2018).
701 Lack of Sp data in the northeast corner of the study region limit our ability to assess the

702 northward limit of negative phase amplitudes as far east as 44°E (Figure 14c). However, some
703 waveform inversion models indicate that very low velocity asthenosphere extends further north
704 at longitudes east of approximately 42°E-43°E, relative to the rest of the study region (Blom et
705 al., 2020; H. Zhu, 2018).

706 The spatial distribution of the negative Sp phase, which appears to mark the base of the
707 asthenospheric low velocity zone, differs from the results of prior Sp studies in the region. The
708 Sp receiver function study by Kind et al. (2015) showed evidence for positive velocity gradients
709 in shallow upper mantle, but the depths where this energy was observed do not always match our
710 results. In Angus et al. (2006), positive velocity gradients were not observed from Sp phases in
711 the 90-150 km depth range. However, much of the region sampled in Angus et al. (2006) lies in
712 eastern Anatolia where the Sp CCP stack presented here shows only a weak positive Sp arrival
713 (e.g. 40°E to 43°E in Figures 10a & 13a), indicating that this study and our results are not
714 incompatible.

715 The anomalously low velocity asthenosphere beneath Anatolia, whose lower margin is indicated
716 by the negative Sp phase, is observed by many seismic studies. In addition to the full-waveform
717 inversion studies described above (Blom et al., 2020; Fichtner et al., 2013; H. Zhu, 2018), low
718 velocity asthenosphere is also observed beneath the Anatolian region by surface wave
719 tomography (Bakırcı et al., 2012; Salaün et al., 2012) and P wave tomography (Portner et al.,
720 2018; Wei et al., 2019). Prior studies also found low Pn wave velocity (Gans et al., 2009; Mutlu
721 & Karabulut, 2011) and high Sn wave attenuation (Gök et al., 2003) beneath a large portion of
722 Anatolia. All of these studies are consistent with anomalously high mantle temperatures, which
723 have also been indicated by multiple geochemical studies (McNab et al., 2018; Nikogosian et al.,
724 2018; Reid et al., 2017). In addition, elevated mantle V_p/V_s ratios (H. Zhu, 2018) as well as the
725 presence of young magmatism (<10 Ma) across the study region (McNab et al., 2018;
726 Nikogosian et al., 2018; Reid et al., 2017) indicate that low velocities in the asthenospheric layer
727 could be enhanced by the presence of partial melt, leading to unusually strong negative Sp
728 energy from the base of this layer. Other regions with a negative Sp arrival in the shallow upper
729 mantle are also often zones of active or recent magmatic activity where the phase could mark the
730 base of a melt-rich mantle layer (e.g. Ford et al., 2014; Hopper et al., 2014; Rychert et al., 2018;
731 Rychert et al., 2013).

732 In contrast to many tectonically active regions with elevated mantle geotherms where a large Sp
733 arrival is observed from the base of the lithosphere (e.g. Fischer et al., 2010; Hansen et al., 2015;
734 Hopper & Fischer, 2018), in Anatolia a strong and ubiquitous phase from the LAB depth range is
735 not evident in the Sp CCP stack obtained with the 4-100 s bandpass filter. In some locations,
736 weak and vertically localized positive Sp phases representing negative velocity gradients are
737 observed directly beneath the Moho (e.g. $\sim 30^\circ\text{E}$ and 38°E in Figure 10a) but they are absent in
738 other areas (e.g. $\sim 28^\circ\text{E}$ in Figure 10a). However, when we instead applied a 2-20 s bandpass
739 filter before deconvolution, stronger and more continuous LAB phases are observed beneath the
740 Moho across most of the Anatolian region at around 60-90 km depth (Figures 15a, S4 & S5).
741 This depth range approximately corresponds to the top of the low velocity asthenosphere layer
742 (e.g. Figures 12 & S2). This observation of a shallow LAB phase is consistent with the depth of
743 the LAB in Kind et al. (2015), but unlike Kind et al. (2015), we observed the strong LAB phase
744 only at relatively short periods. In addition, the relative amplitude of the LAB phases in this
745 study is low compared to those in Kind et al. (2015), where LAB phase amplitudes are
746 sometimes comparable to Moho phases.

747 A possible reason for LAB phases to be weak or absent when using 4-100 s filter is that the
748 mantle lithosphere is too thin to be resolved by long wavelength body waves. In other words, the
749 LAB phase is reduced by interference with a larger Moho phase. To test this hypothesis, a
750 numerical experiment was designed with propagator matrix synthetic seismograms. For velocity
751 structures with varying mantle lithospheric thicknesses (Figure 16a), synthetic S waves with the
752 same ray parameter (0.1098 s/km) were recorded by a station at the surface. However, some
753 waves had Gaussian first derivative source time functions with a period of 14 s (~ 0.07 Hz), while
754 the others had dominant periods of 4 s (0.25 Hz), and bandpass filters of 4-100 s and 2-20 s were
755 applied. Synthetic seismograms were then deconvolved to obtain Sp receiver functions, using
756 the same approach that was applied to the data, and receiver functions were migrated to depth
757 (Figure 16a). When the mantle lithosphere is thinner than 10 km, LAB phases can barely be
758 observed for any filter or dominant period. When mantle lithosphere thickness is more than 10
759 km but less than 30 km, receiver functions with 4 s source time functions better capture LAB
760 phases with correct depths and stronger amplitudes. When mantle lithosphere thickness is
761 approximately 30 km, 4 s and 14 s receiver functions are similar. These synthetic tests indicate
762 that higher frequency seismograms better resolve LAB phases when mantle lithosphere is thin.

763 When using a 4-100 s bandpass filter with real data, S phases with periods even longer than 14 s
764 are also included, making the LAB even more difficult to observe than in the numerical
765 experiment. The 2-20 s bandpass filter does not significantly alter receiver functions with short-
766 period source time functions compared to the 4-100 s bandpass filter (e.g. middle-right versus
767 middle-left panel in Figure 16a), but it eliminates longer period waveforms that obscure the LAB
768 phase.

769 However, while the observed LAB phases become more prominent when using 2-20 s filter, the
770 positive velocity gradient phases are relatively weaker with this filter compared to the 4-100 s
771 bandpass (e.g. Figure 15a versus Figure 10a). To better understand this frequency dependence,
772 another synthetic experiment was designed with a similar setup to the former case, but with a
773 lithospheric thickness fixed at 15 km, and a shear velocity increase from 4.0 km/s to 4.4 km/s
774 centered at 120 km depth. The latter is distributed over a depth range as narrow as 10 km and as
775 broad as 45 km (Figure 16b). When a 4-100 s bandpass filter was applied, receiver functions
776 from a 4 s source time functions are more sensitive to the depth range of the velocity increase
777 when the depth range is more than 30 km, while the 14 s receiver functions show less amplitude
778 variation (middle-left versus left-most panel in Figure 16b). However, when a 2-20 s filter was
779 applied, positive velocity gradient phases become much weaker for 4 s receiver functions from
780 velocity gradients broader than 30 km (middle-right versus middle-left panel in Figure 16b).
781 This result is because the long period Green's functions for converted waves originating from the
782 gradual velocity increase are filtered out.

783 Based on this synthetic test, and the larger amplitude of the observed positive phase from the
784 base of the asthenosphere with the 4-100 s filter relative to the 2-20 s, we conclude that the
785 corresponding positive velocity gradient is likely distributed over a depth extent of at least 30
786 km. However, if the velocity gradient is distributed over more than 30 km, the synthetics
787 indicate that the amplitude of the phase should continue to increase as the dominant period in the
788 waveforms further increases, for example the 14 s source versus the 4 s source with the 4-100 s
789 filter (middle-left versus left-most panel in Figure 16b). To produce a shift to longer dominant
790 periods, we also performed the CCP stacking with Sp receiver functions from seismograms with
791 a 10-100 s bandpass filter (Figure 15b, S6 & S7). The positive velocity gradient phase in this
792 case is in many places stronger than in the 4-100 s case, especially for profile B-B' (Figure S6a

793 versus Figure 13a), suggesting that the velocity gradient is probably more gradual than a 30 km
794 depth extent.

795 These synthetic tests show that in order to observe both thin mantle lithosphere and the gradual
796 positive velocity gradient at the base of the low velocity asthenospheric layer, the best choice is
797 to use seismograms with short-period source time functions and filter them with broad bandpass
798 filters (e.g. the cases with a 4 s source time function and a 4-100 s filter in Figure 16). However,
799 with real data, a shorter period filter is often necessary to isolate short period source time
800 function seismograms, and it is key to construct receiver function stacks with different frequency
801 bands to resolve thin layers and velocity gradient depth ranges.

802

803 **5. Conclusions**

804 A new approach to finding free-surface velocities from the polarizations of P and S arrivals was
805 developed. This approach has the ability to accurately measure the shear velocity from P arrivals
806 and compressional velocity from S arrivals both with synthetic data and real data. With the
807 retrieved free-surface velocities, P and SV components of seismograms are isolated successfully,
808 resulting in clear Sp receiver functions.

809 Receiver functions were accurately mapped to depth with a novel kernel-based CCP stacking
810 method. Instead of using empirically defined weighting functions or geographic bins, the new
811 method focuses imaging the horizontal discontinuities assumed in CCP stacking using the shape
812 of scattering kernels. Receiver function amplitudes are projected into the stack using weighting
813 functions that highlight locations where the kernel is relatively flat, its depth offset from the
814 conversion point is minimal, and geometric spreading is small. With typical upper mantle
815 seismic velocities, Sp weighting functions span much broader horizontal regions than Ps
816 weighting functions, indicating an advantage for Sp receiver functions when imaging quasi-
817 horizontal structures.

818 A fast and accurate approach to quantifying the standard deviation of CCP stacking results is
819 derived based on the central limit theorem. The estimated standard deviation requires only one
820 quick calculation, but is very close to the value obtained by bootstrapping after the latter

821 converges over thousands of iterations. The derived expression can be applied to all problems
822 requiring a standard deviation of weighted averages, and it requires neither the sum of weights to
823 be constant nor the weight to be independent of the sample.

824 Sp receiver function CCP stacking, after careful quality control, resulted in clear images of upper
825 mantle discontinuities beneath the Anatolian region. Using waveforms with periods of 4-100 s,
826 the Moho, the 410-discontinuity, a velocity decrease at depths of 360-380 km, and a prominent
827 positive velocity gradient located between 80 and 150 km depth are observed. The latter positive
828 velocity gradient marks the base of a low velocity asthenospheric layer which appears in
829 numerous prior models of the Anatolian upper mantle. Causes of the pronounced low velocity
830 asthenosphere could be high mantle temperature or the presence of partial melt, which are also
831 indicated by previous geochemical and seismological studies. While the strong positive velocity
832 gradient is observed beneath most of the region, it does not extend far beyond the North
833 Anatolian Fault in western and central-eastern Anatolia, suggesting a relationship between the
834 plate boundary and its hot underlying asthenospheric mantle.

835 Strong Sp phases from a negative velocity gradient that corresponds to the LAB are not clearly
836 observed in the CCP stack that employed receiver functions with a 4-100 s bandpass filters, but
837 an LAB Sp phase was clearly imaged at 60 to 90 km depth with a 2-20 s filter. Tests with
838 synthetic seismograms show that this frequency dependent behavior is expected with thin mantle
839 lithosphere. This phase is consistent with the upper margin of the low velocity asthenosphere.

840 Frequency dependence in the amplitude of the Sp phases from the base of the asthenospheric low
841 velocity layer places constraints on the depth extent of its velocity gradient. The Sp phase
842 amplitude is clearly smallest in the CCP stack with the 2-20 s bandpass filter, indicating that the
843 positive velocity gradient occurs over more than 30 km in depth. Beneath much of the region,
844 southern portions of western and central Anatolia in particular, the amplitude of the phase is
845 larger in the CCP stack with a 10-100 s bandpass filter relative to the stack with the 4-100 s
846 bandpass filter, indicating that the depth extent of the velocity gradient is even larger.

847 **Acknowledgements**

848 Seismograms were downloaded either through IRIS Data Management Center BREQ_FAST
849 service or through obspyDMT toolbox (Hosseini & Sigloch, 2017) for data managed by other

850 data centers supporting FDSN Web Services. Waveforms were collected by 11 permanent
 851 networks (KO, <https://doi.org/10.7914/SN/KO>; GE, <https://doi.org/10.14470/TR560404>; HL,
 852 <https://doi.org/10.7914/SN/HL>; TU; CQ, <https://doi.org/10.7914/SN/CQ>; HT,
 853 <https://doi.org/10.7914/SN/HT>; GO; HC, <https://doi.org/10.7914/SN/HC>; MN,
 854 <https://doi.org/10.13127/SD/fBBBtDtd6q>; IU, <https://doi.org/10.7914/SN/IU>; AB) and 14
 855 temporary networks (YB, https://doi.org/10.7914/SN/YB_2013; YL,
 856 https://doi.org/10.7914/SN/YL_2005; YI, <https://doi.org/10.15778/RESIF.YI2008>; XW,
 857 <https://doi.org/10.15778/RESIF.XW2007>; XY, <https://doi.org/10.15778/RESIF.XY2007>; Z3,
 858 <https://doi.org/10.14470/M87550267382>; ZZ, <https://doi.org/10.14470/MM7557265463>; XO;
 859 XH, https://doi.org/10.7914/SN/XH_2002; YF; TK; SU; SD). Our thanks to D. Friedman for
 860 initial data downloading. Our thanks to A. Fichtner for providing the velocity model of Fichtner
 861 et al. (2013) and discussion, and to T. Bakırcı for discussion. This work was supported by the U.
 862 S. National Science Foundation through awards EAR-1416753 and EAR-1829401.

863

864 References

- 865 Abgarni, B., Delph, J. R., Ozacar, A. A., Beck, S. L., Zandt, G., Sandvol, E., et al. (2017). Structure of the crust and
 866 African slab beneath the central Anatolian plateau from receiver functions: New insights on isostatic
 867 compensation and slab dynamics. *Geosphere*, 13(6), 1774-1787. <https://doi.org/10.1130/GES01509.1>
 868 Abt, D. L., Fischer, K. M., French, S. W., Ford, H. A., Yuan, H., & Romanowicz, B. (2010). North American
 869 lithospheric discontinuity structure imaged by Ps and Sp receiver functions. *Journal of Geophysical*
 870 *Research: Solid Earth*, 115(B9). <https://doi.org/10.1029/2009JB006914>
 871 Aki, K., & Richards, P. G. (2002). *Quantitative seismology* (2nd ed.): University Science Books.
 872 Angus, D., Wilson, D. C., Sandvol, E., & Ni, J. (2006). Lithospheric structure of the Arabian and Eurasian collision
 873 zone in eastern Turkey from S-wave receiver functions. *Geophysical Journal International*, 166(3), 1335-
 874 1346. <https://doi.org/10.1111/j.1365-246X.2006.03070.x>
 875 Bakırcı, T., Yoshizawa, K., & Özer, M. F. (2012). Three-dimensional S-wave structure of the upper mantle beneath
 876 Turkey from surface wave tomography. *Geophysical Journal International*, 190(2), 1058-1076.
 877 <https://doi.org/10.1111/j.1365-246X.2012.05526.x>
 878 Berk Biryol, C., Beck, S. L., Zandt, G., & Özacar, A. A. (2011). Segmented African lithosphere beneath the
 879 Anatolian region inferred from teleseismic P-wave tomography. *Geophysical Journal International*, 184(3),
 880 1037-1057. <https://doi.org/10.1111/j.1365-246X.2010.04910.x>
 881 Blom, N., Gokhberg, A., & Fichtner, A. (2020). Seismic waveform tomography of the Central and Eastern
 882 Mediterranean upper mantle. *Solid Earth*, 11(2), 669-690. <https://doi.org/10.5194/se-11-669-2020>
 883 Bostock, M. G., & Rondenay, S. (1999). Migration of scattered teleseismic body waves. *Geophysical Journal*
 884 *International*, 137(3), 732-746. <https://doi.org/10.1046/j.1365-246x.1999.00813.x>
 885 Bostock, M. G., Rondenay, S., & Shragge, J. (2001). Multiparameter two-dimensional inversion of scattered
 886 teleseismic body waves 1. Theory for oblique incidence. *Journal of Geophysical Research Solid Earth*,
 887 106(B12), 30771-30782. <https://doi.org/10.1029/2001JB000330>
 888 Cramer, F. (2018). Geodynamic diagnostics, scientific visualisation and StagLab 3.0. *Geoscientific Model*
 889 *Development*, 11(6), 2541-2562. <https://doi.org/10.5194/gmd-11-2541-2018>

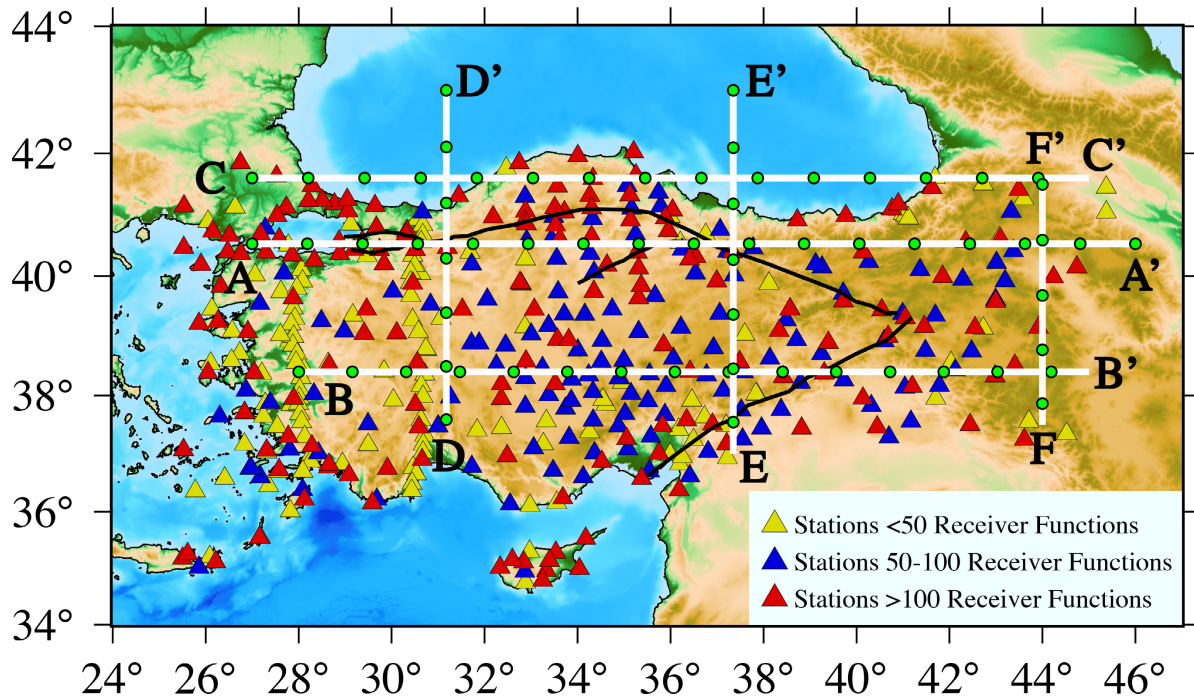
- 890 Delph, J. R., Biryol, C. B., Beck, S. L., Zandt, G., & Ward, K. M. (2015). Shear wave velocity structure of the
891 Anatolian Plate: anomalously slow crust in southwestern Turkey. *Geophysical Journal International*,
892 202(1), 261-276. <https://doi.org/10.1093/gji/ggv141>
- 893 Dueker, K. G., & Sheehan, A. F. (1997). Mantle discontinuity structure from midpoint stacks of converted P to S
894 waves across the Yellowstone hotspot track. *Journal of Geophysical Research: Solid Earth*, 102(B4), 8313-
895 8327.
- 896 Faccenna, C., Bellier, O., Martinod, J., Piromallo, C., & Regard, V. (2006). Slab detachment beneath eastern
897 Anatolia: A possible cause for the formation of the North Anatolian fault. *Earth and Planetary Science*
898 *Letters*, 242(1-2), 85-97. <https://doi.org/10.1016/j.epsl.2005.11.046>
- 899 Farra, V., & Vinnik, L. (2000). Upper mantle stratification by P and S receiver functions. *Geophysical Journal*
900 *International*, 141(3), 699-712. <https://doi.org/10.1046/j.1365-246x.2000.00118.x>
- 901 Fichtner, A., Saygin, E., Taymaz, T., Cupillard, P., Capdeville, Y., & Trampert, J. (2013). The deep structure of the
902 North Anatolian Fault Zone. *Earth and Planetary Science Letters*, 373, 109-117.
903 <https://doi.org/10.1016/j.epsl.2013.04.027>
- 904 Fischer, K. M., Ford, H. A., Abt, D. L., & Rychert, C. A. (2010). The lithosphere-asthenosphere boundary. *Annual*
905 *Review of Earth and Planetary Sciences*, 38, 551-575. [https://doi.org/10.1146/annurev-earth-040809-
906 152438](https://doi.org/10.1146/annurev-earth-040809-152438)
- 907 Ford, H. A., Fischer, K. M., & Lekic, V. (2014). Localized shear in the deep lithosphere beneath the San Andreas
908 fault system. *Geology*, 42(4), 295-298. <https://doi.org/10.1130/G35128.1>
- 909 Frederiksen, A. W., Thompson, D. A., Rost, S., Cornwell, D. G., Gülen, L., Houseman, G. A., et al. (2015). Crustal
910 thickness variations and isostatic disequilibrium across the North Anatolian Fault, western Turkey.
911 *Geophysical Research Letters*, 42(3), 751-757. <https://doi.org/10.1002/2014GL062401>
- 912 Gans, C. R., Beck, S. L., Zandt, G., Biryol, C. B., & Ozacar, A. A. (2009). Detecting the limit of slab break-off in
913 central Turkey: new high-resolution Pn tomography results. *Geophysical Journal International*, 179(3),
914 1566-1572. <https://doi.org/10.1111/j.1365-246X.2009.04389.x>
- 915 Gök, R., Sandvol, E., Türkelli, N., Seber, D., & Barazangi, M. (2003). Sn attenuation in the Anatolian and Iranian
916 plateau and surrounding regions. *Geophysical Research Letters*, 30(24).
917 <https://doi.org/10.1029/2003GL018020>
- 918 Govers, R., & Fichtner, A. (2016). Signature of slab fragmentation beneath Anatolia from full-waveform
919 tomography. *Earth and Planetary Science Letters*, 450, 10-19. <https://doi.org/10.1016/j.epsl.2016.06.014>
- 920 Hannemann, K., Krüger, F., Dahm, T., & Lange, D. (2016). Oceanic lithospheric S-wave velocities from the
921 analysis of P-wave polarization at the ocean floor. *Geophysical Supplements to the Monthly Notices of the*
922 *Royal Astronomical Society*, 207(3), 1796-1817. <https://doi.org/10.1093/gji/ggw342>
- 923 Hansen, S. M., Dueker, K., & Schmandt, B. (2015). Thermal classification of lithospheric discontinuities beneath
924 USArray. *Earth and Planetary Science Letters*, 431, 36-47. <https://doi.org/10.1016/j.epsl.2015.09.009>
- 925 Hansen, S. M., & Schmandt, B. (2017). P and S wave receiver function imaging of subduction with scattering
926 kernels. *Geochemistry, Geophysics, Geosystems*, 18(12), 4487-4502.
927 <https://doi.org/10.1002/2017GC007120>
- 928 Hopper, E., & Fischer, K. M. (2018). The changing face of the lithosphere-asthenosphere boundary: Imaging
929 continental scale patterns in upper mantle structure across the contiguous US with Sp converted waves.
930 *Geochemistry, Geophysics, Geosystems*, 19(8), 2593-2614. <https://doi.org/10.1029/2018GC007476>
- 931 Hopper, E., Ford, H. A., Fischer, K. M., Lekic, V., & Fouch, M. J. (2014). The lithosphere-asthenosphere boundary
932 and the tectonic and magmatic history of the northwestern United States. *Earth and Planetary Science*
933 *Letters*, 402, 69-81. <https://doi.org/10.1016/j.epsl.2013.12.016>
- 934 Hosseini, K., & Sigloch, K. (2017). obspyDMT: a Python toolbox for retrieving and processing of large
935 seismological datasets. *Solid Earth*, 8. <https://doi.org/10.5194/se-8-1047-2017>
- 936 Hua, J., Fischer, K. M., Mancinelli, N. J., & Bao, T. (2020). Imaging with pre-stack migration based on Sp
937 scattering kernels. *Geophysical Journal International*, 220(1), 428-449. <https://doi.org/10.1093/gji/ggz459>
- 938 Hua, J., Fischer, K. M., & Savage, M. K. (2018). The lithosphere-asthenosphere boundary beneath the South Island
939 of New Zealand. *Earth and Planetary Science Letters*, 484, 92-102.
940 <https://doi.org/10.1016/j.epsl.2017.12.011>
- 941 Jolivet, L., Faccenna, C., Huet, B., Labrousse, L., Le Pourhiet, L., Lacombe, O., et al. (2013). Aegean tectonics:
942 Strain localisation, slab tearing and trench retreat. *Tectonophysics*, 597-598, 1-33.
943 <https://doi.org/10.1016/j.tecto.2012.06.011>

- 944 Kandilli Observatory and Earthquake Research Institute Bosphorus Univ. (2001). *Bogazici University Kandilli*
 945 *Observatory And Earthquake Research Institute*. International Federation of Digital Seismograph
 946 Networks. Dataset/Seismic Network.
- 947 Karabulut, H., Paul, A., Özbakır, A. D., Ergün, T., & Şentürk, S. (2019). A new crustal model of the Anatolia–
 948 Aegean domain: evidence for the dominant role of isostasy in the support of the Anatolian plateau.
 949 *Geophysical Journal International*, 218(1), 57-73. <https://doi.org/10.1093/gji/ggz147>
- 950 Keith, C. M., & Crampin, S. (1977). Seismic body waves in anisotropic media: synthetic seismograms. *Geophysical*
 951 *Journal International*, 49(1), 225-243.
- 952 Kennett, B. L. (1991). The removal of free surface interactions from three-component seismograms. *Geophysical*
 953 *Journal International*, 104(1), 153-154. <https://doi.org/10.1111/j.1365-246X.1991.tb02501.x>
- 954 Kennett, B. L., Engdahl, E., & Buland, R. (1995). Constraints on seismic velocities in the Earth from traveltimes.
 955 *Geophysical Journal International*, 122(1), 108-124. <https://doi.org/10.1111/j.1365-246X.1995.tb03540.x>
- 956 Keskin, M. (2003). Magma generation by slab steepening and breakoff beneath a subduction-accretion complex: An
 957 alternative model for collision-related volcanism in Eastern Anatolia, Turkey. *Geophysical Research*
 958 *Letters*, 30(24). <https://doi.org/10.1029/2003GL018019>
- 959 Kind, R., Eken, T., Tilmann, F., Sodoudi, F., Taymaz, T., Bulut, F., et al. (2015). Thickness of the lithosphere
 960 beneath Turkey and surroundings from S-receiver functions. *Solid Earth*, 6(3), 971-984.
 961 <https://doi.org/10.5194/se-6-971-2015>
- 962 Kind, R., Yuan, X., & Kumar, P. (2012). Seismic receiver functions and the lithosphere–asthenosphere boundary.
 963 *Tectonophysics*, 536, 25-43. <https://doi.org/10.1016/j.tecto.2012.03.005>
- 964 Lekić, V., & Fischer, K. M. (2014). Contrasting lithospheric signatures across the western United States revealed by
 965 Sp receiver functions. *Earth and Planetary Science Letters*, 402, 90-98.
 966 <https://doi.org/10.1016/j.epsl.2013.11.026>
- 967 Lekić, V., & Fischer, K. M. (2017). Interpreting spatially stacked Sp receiver functions. *Geophysical Journal*
 968 *International*, 210(2), 874-886. <https://doi.org/10.1093/gji/ggx206>
- 969 Lekic, V., French, S. W., & Fischer, K. M. (2011). Lithospheric thinning beneath rifted regions of southern
 970 California. *Science*, 334(6057), 783-787. <https://doi.org/10.1126/science.1208898>
- 971 Licciardi, A., Eken, T., Taymaz, T., Agostinetti, N. P., & Yolsal-Çevikbilen, S. (2018). Seismic anisotropy in central
 972 North Anatolian Fault Zone and its implications on crustal deformation. *Physics of the Earth and Planetary*
 973 *Interiors*, 277, 99-112. <https://doi.org/10.1016/j.pepi.2018.01.012>
- 974 Ligorria, J. P., & Ammon, C. J. (1999). Iterative deconvolution and receiver-function estimation. *Bulletin of the*
 975 *seismological Society of America*, 89(5), 1395-1400.
- 976 Mancinelli, N., & Fischer, K. (2017). The spatial sensitivity of Sp converted waves—scattered-wave kernels and
 977 their applications to receiver-function migration and inversion. *Geophysical Journal International*, 212(3),
 978 1722-1735. <https://doi.org/10.1093/gji/ggx506>
- 979 McNab, F., Ball, P. W., Hoggard, M. J., & White, N. J. (2018). Neogene Uplift and Magmatism of Anatolia:
 980 Insights From Drainage Analysis and Basaltic Geochemistry. *Geochemistry, Geophysics, Geosystems*,
 981 19(1), 175-213. <https://doi.org/10.1002/2017GC007251>
- 982 Mutlu, A. K., & Karabulut, H. (2011). Anisotropic Pn tomography of Turkey and adjacent regions. *Geophysical*
 983 *Journal International*, 187(3), 1743-1758. 10.1111/j.1365-246X.2011.05235.x
- 984 Nikogosian, I., Gartner, A. B., van Bergen, M., Mason, P., & Van Hinsbergen, D. J. (2018). Mantle sources of
 985 recent Anatolian intraplate magmatism: A regional plume or local tectonic origin? *Tectonics*, 37(12), 4535-
 986 4566. <https://doi.org/10.1029/2018TC005219>
- 987 Ozacar, A. A., Gilbert, H., & Zandt, G. (2008). Upper mantle discontinuity structure beneath East Anatolian Plateau
 988 (Turkey) from receiver functions. *Earth and Planetary Science Letters*, 269(3-4), 427-435.
 989 <https://doi.org/10.1016/j.epsl.2008.02.036>
- 990 Park, S., & Ishii, M. (2018). Near-surface compressional and shear wave speeds constrained by body-wave
 991 polarization analysis. *Geophysical Journal International*, 213(3), 1559-1571.
 992 <https://doi.org/10.1093/gji/ggy072>
- 993 Park, S., Tsai, V. C., & Ishii, M. (2019). Frequency-Dependent P Wave Polarization and Its Subwavelength Near-
 994 Surface Depth Sensitivity. *Geophysical Research Letters*. <https://doi.org/10.1029/2019GL084892>
- 995 Portner, D. E., Delph, J. R., Biryol, C. B., Beck, S. L., Zandt, G., Özacar, A. A., et al. (2018). Subduction
 996 termination through progressive slab deformation across Eastern Mediterranean subduction zones from
 997 updated P-wave tomography beneath Anatolia. *Geosphere*, 14(3), 907-925.
 998 <https://doi.org/10.1130/GES01617.1>

- 999 Reid, M. R., Schleiffarth, W. K., Cosca, M. A., Delph, J. R., Blichert-Toft, J., & Cooper, K. M. (2017). Shallow
1000 melting of MORB-like mantle under hot continental lithosphere, Central Anatolia. *Geochemistry,*
1001 *Geophysics, Geosystems, 18*(5), 1866-1888. <https://doi.org/10.1002/2016GC006772>
- 1002 Reilinger, R., McClusky, S., Vernant, P., Lawrence, S., Ergintav, S., Cakmak, R., et al. (2006). GPS constraints on
1003 continental deformation in the Africa-Arabia-Eurasia continental collision zone and implications for the
1004 dynamics of plate interactions. *Journal of Geophysical Research: Solid Earth, 111*(B5).
1005 <https://doi.org/10.1029/2005JB004051>
- 1006 Rondenay, S. (2009). Upper mantle imaging with array recordings of converted and scattered teleseismic waves.
1007 *Surveys in Geophysics, 30*(4-5), 377-405. <https://doi.org/10.1007/s10712-009-9071-5>
- 1008 Rondenay, S., Bostock, M. G., & Fischer, K. M. (2005). Multichannel inversion of scattered teleseismic body
1009 waves: Practical considerations and applicability. *Washington Dc American Geophysical Union*
1010 *Geophysical Monograph, 157*, 187-203. <https://doi.org/10.1029/157GM12>
- 1011 Rychert, C. A., Harmon, N., & Tharimena, S. (2018). Scattered wave imaging of the oceanic plate in Cascadia.
1012 *Science advances, 4*(2), eaao1908. <https://doi.org/10.1126/sciadv.aao1908>
- 1013 Rychert, C. A., Laske, G., Harmon, N., & Shearer, P. M. (2013). Seismic imaging of melt in a displaced Hawaiian
1014 plume. *Nature Geoscience, 6*(8), 657-660. <https://doi.org/10.1038/ngeo1878>
- 1015 Salaün, G., Pedersen, H. A., Paul, A., Farra, V., Karabulut, H., Hatzfeld, D., et al. (2012). High-resolution surface
1016 wave tomography beneath the Aegean-Anatolia region: constraints on upper-mantle structure. *Geophysical*
1017 *Journal International, 190*(1), 406-420. <https://doi.org/10.1111/j.1365-246X.2012.05483.x>
- 1018 Schildgen, T. F., Yildirim, C., Cosentino, D., & Strecker, M. R. (2014). Linking slab break-off, Hellenic trench
1019 retreat, and uplift of the Central and Eastern Anatolian plateaus. *Earth-Science Reviews, 128*, 147-168.
1020 <https://doi.org/10.1016/j.earscirev.2013.11.006>
- 1021 Şengör, A., Özeren, S., Genç, T., & Zor, E. (2003). East Anatolian high plateau as a mantle-supported, north-south
1022 shortened domal structure. *Geophysical Research Letters, 30*(24). <https://doi.org/10.1029/2003GL017858>
- 1023 Şengör, A. M. C., Özeren, M. S., Keskin, M., Sakıncı, M., Özbakır, A. D., & Kayan, İ. (2008). Eastern Turkish high
1024 plateau as a small Turkic-type orogen: Implications for post-collisional crust-forming processes in Turkic-
1025 type orogens. *Earth-Science Reviews, 90*(1-2), 1-48. <https://doi.org/10.1016/j.earscirev.2008.05.002>
- 1026 Sverningesen, L., & Jacobsen, B. (2007). Absolute S-velocity estimation from receiver functions. *Geophysical*
1027 *Journal International, 170*(3), 1089-1094. <https://doi.org/10.1111/j.1365-246X.2006.03505.x>
- 1028 Vanacore, E. A., Taymaz, T., & Saygin, E. (2013). Moho structure of the Anatolian Plate from receiver function
1029 analysis. *Geophysical Journal International, 193*(1), 329-337. <https://doi.org/10.1093/gji/ggs107>
- 1030 Vinnik, L., & Farra, V. (2002). Subcratonic low-velocity layer and flood basalts. *Geophysical Research Letters,*
1031 *29*(4), 8-1-8-4. <https://doi.org/10.1029/2001GL014064>
- 1032 Wei, W., Zhao, D., Wei, F., Bai, X., & Xu, J. (2019). Mantle Dynamics of the Eastern Mediterranean and Middle
1033 East: Constraints From P-Wave Anisotropic Tomography. *Geochemistry, Geophysics, Geosystems, 20*(10),
1034 4505-4530. <https://doi.org/10.1029/2019GC008512>
- 1035 Wiechert, E., & Zoeppritz, K. (1907). Über erdbebenwellen. *Nachrichten von der Gesellschaft der Wissenschaften*
1036 *zu Göttingen, Mathematisch-Physikalische Klasse, 1907*, 415-549.
- 1037 Wittlinger, G., & Farra, V. (2007). Converted waves reveal a thick and layered tectosphere beneath the Kalahari
1038 super-craton. *Earth and Planetary Science Letters, 254*(3-4), 404-415.
1039 <https://doi.org/10.1016/j.epsl.2006.11.048>
- 1040 Yuan, X., Kind, R., Li, X., & Wang, R. (2006). The S receiver functions: synthetics and data example. *Geophysical*
1041 *Journal International, 165*(2), 555-564. <https://doi.org/10.1111/j.1365-246X.2006.02885.x>
- 1042 Zhang, H., & Schmandt, B. (2019). Application of Ps Scattering Kernels to Imaging the Mantle Transition Zone
1043 with Receiver Functions. *Journal of Geophysical Research: Solid Earth.*
1044 <https://doi.org/10.1029/2018JB016274>
- 1045 Zhu, H. (2018). High Vp/Vs ratio in the crust and uppermost mantle beneath volcanoes in the Central and Eastern
1046 Anatolia. *Geophysical Journal International, 214*(3), 2151-2163. <https://doi.org/10.1093/gji/ggy253>
- 1047 Zhu, L., Mitchell, B. J., Akyol, N., Cemen, I., & Kekovali, K. (2006). Crustal thickness variations in the Aegean
1048 region and implications for the extension of continental crust. *Journal of Geophysical Research: Solid*
1049 *Earth, 111*(B1). <https://doi.org/10.1029/2005JB003770>
- 1050 Zor, E., Sandvol, E., Gürbüz, C., Türkelli, N., Seber, D., & Barazangi, M. (2003). The crustal structure of the East
1051 Anatolian plateau (Turkey) from receiver functions. *Geophysical Research Letters, 30*(24).
1052 <https://doi.org/10.1029/2003GL018192>
- 1053

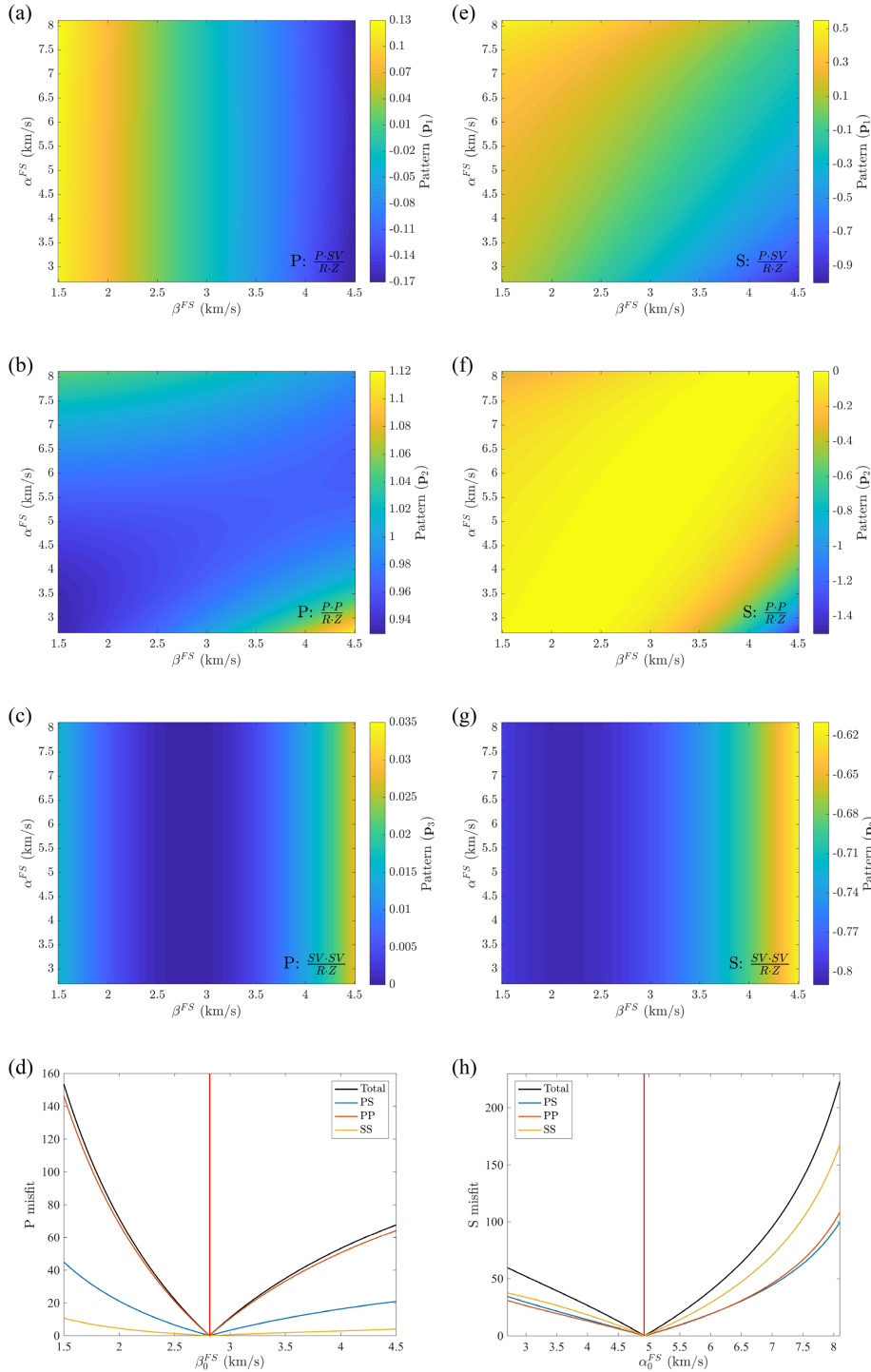
1054 **Figures:**

1055



1056

1057 **Figure 1.** Map of the study region covering the Anatolian Plate. Broadband stations employed in
 1058 this study are triangles; stations with less than 50 Sp receiver functions are shown in yellow
 1059 color, those with 50 to 100 receiver functions are in blue, and those with more than 100 receiver
 1060 functions are in red. The North Anatolian Fault and East Anatolian Fault are shown by black
 1061 lines. Bold white are the locations of profiles discussed in this paper; the distance between the
 1062 green circles is 100 km.



1063

1064

1065

1066

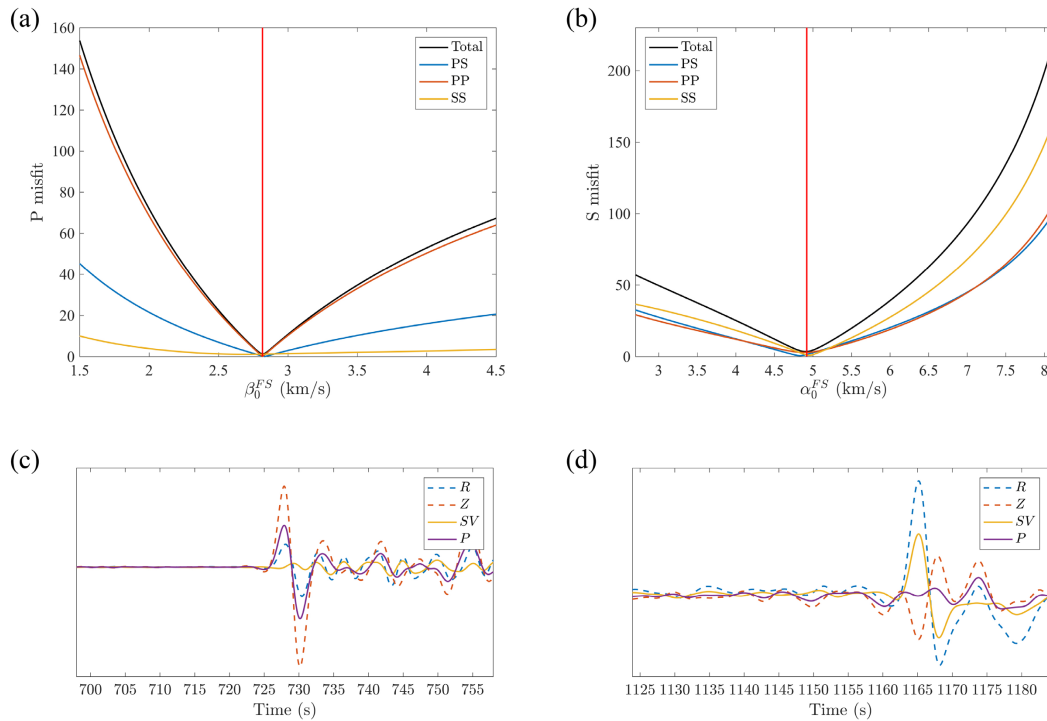
1067

1068

Figure 2. Particle motion patterns in equation (4) obtained with synthetic seismograms generated for a half space with $V_p=4.92$ km/s and $V_s=2.82$ km/s. (a) The pattern C_1 in equation (4) for a P arrival with a ray parameter of 0.0482 s/km. Colors show the value of the pattern for varying α^{FS} and β^{FS} . The label at the bottom right corner indicates the arrival phase and the equation for the pattern. (b)-(c) similar to (a), but for C_2 and C_3 . (d) Determination of β_0^{FS} by

1069 minimizing the misfit function defined in section 2.1. The black curve shows the value of the
 1070 total misfit function defined in equation (6) for different β_0^{FS} , the blue curve shows the value
 1071 when the misfit function is defined as $\|C_1 - C_1^p\|_2$, the red curve is for misfit function $\|C_2 - C_2^p\|_2$,
 1072 and the yellow curve is for misfit function $\|C_3 - C_3^p\|_2$. C_2 makes the largest contribution to the
 1073 total misfit. The vertical red line shows the true β_0^{FS} from the structure used to calculate the
 1074 synthetic waveforms. (e)-(g) similar to (a)-(c) but for an S-arrival with a ray parameter of 0.1098
 1075 s/km. (h) similar to (d) but searching for α_0^{FS} ; the vertical red line indicates the true α_0^{FS} .

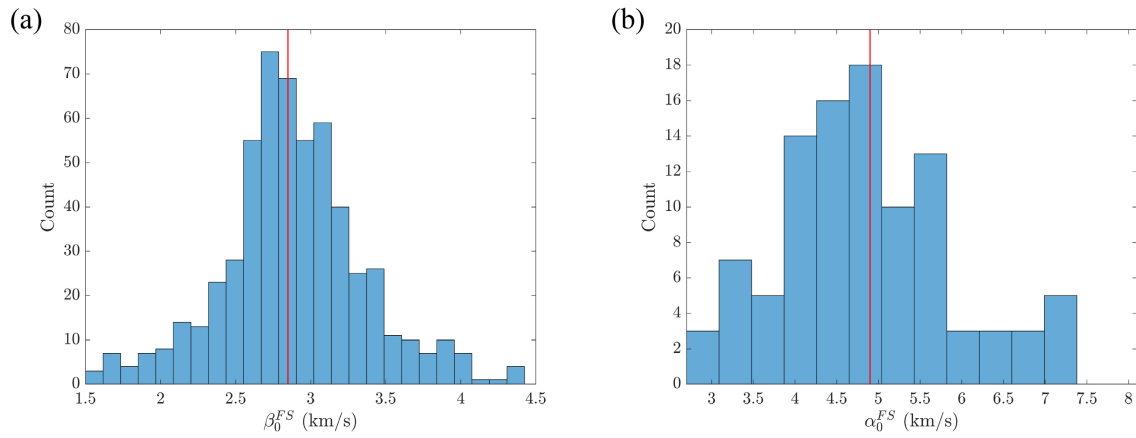
1076



1077

1078 **Figure 3.** (a) Plot similar to Figure 2d and (b) plot similar to Figure 2h but using records from
 1079 two real events. Both the P arrival event and the S arrival event have the same ray parameters as
 1080 those used in the synthetic case in Figure 2. Colors and curves are defined identically to those in
 1081 Figure 2. The only difference is the vertical red lines show the β_0^{FS} and α_0^{FS} values obtained by
 1082 minimizing the misfit function in equation (6); their values are equal to the half space velocities
 1083 used in Figure 2. (c) P and SV component example for the real P arrival used in (a). The x-axis
 1084 is time from the earthquake origin time. Blue and red dashed lines show the radial and vertical
 1085 components of the seismogram, and yellow and purple lines are the P and SV components based
 1086 on equation (1) and the determined β_s^{FS} and α_s^{FS} values. (d) Similar to (c), but for the real S
 1087 arrival used in (b).

1088



1089

1090 **Figure 4.** (a) Histogram of β_0^{FS} values obtained from 562 individual P-arrivals whose weight for
 1091 free surface velocity calculation is not zero. The bin width is 0.117 km/s. The red line shows the
 1092 final determined β_s^{FS} from the weighted average of individual β_0^{FS} . (b) Similar to (a) but with
 1093 results for α_0^{FS} from 100 individual S-arrivals. The bin width is 0.39 km/s.

1094

1095

1096

1097

1098

1099

1100

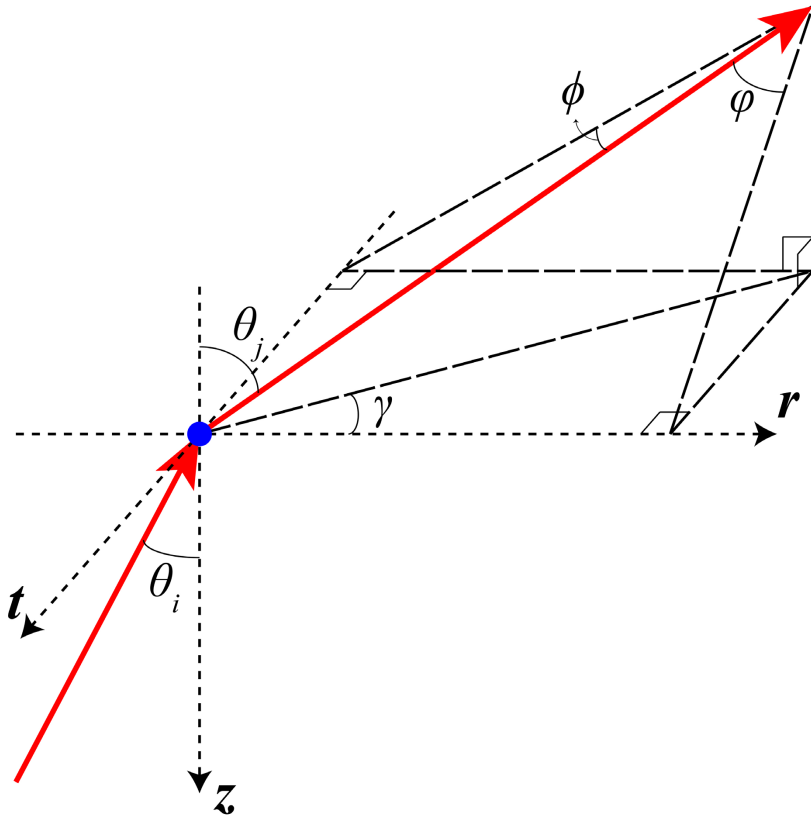
1101

1102

1103

1104

1105



1106

1107 **Figure 5.** Schematic plot of the scattering process. Ray paths of the incident wave propagating in
 1108 the r - z plane and the scattered wave are shown by red lines. The scatterer is marked by the blue
 1109 dot. The coordinates and angles used for calculating the phase delay time isochron slope angle
 1110 are also labelled.

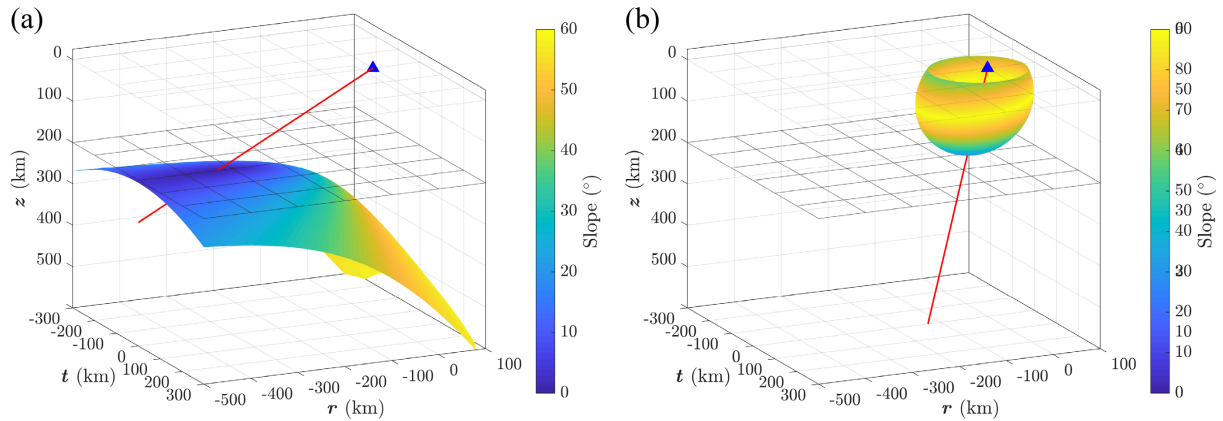
1111

1112

1113

1114

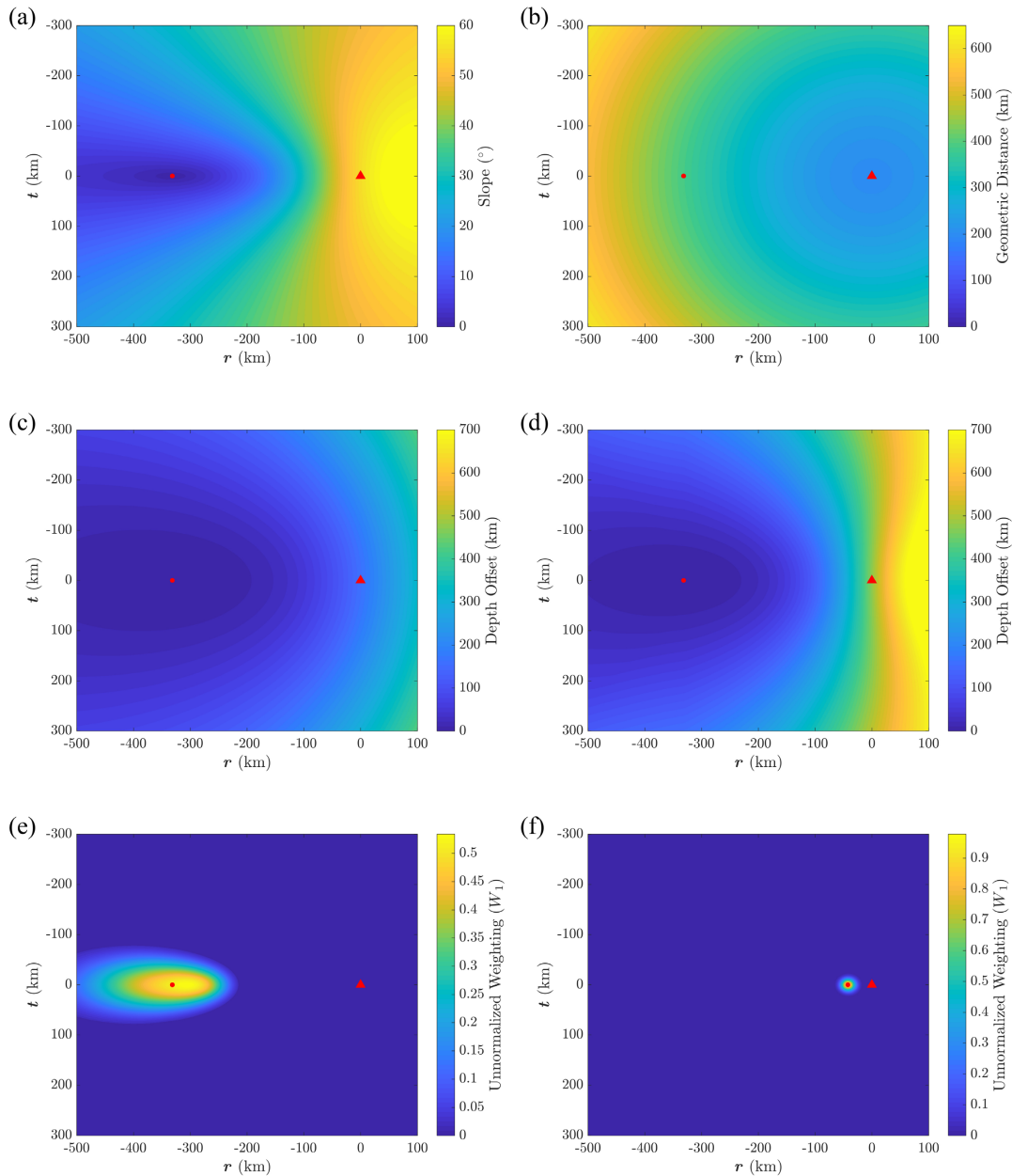
1115



1116

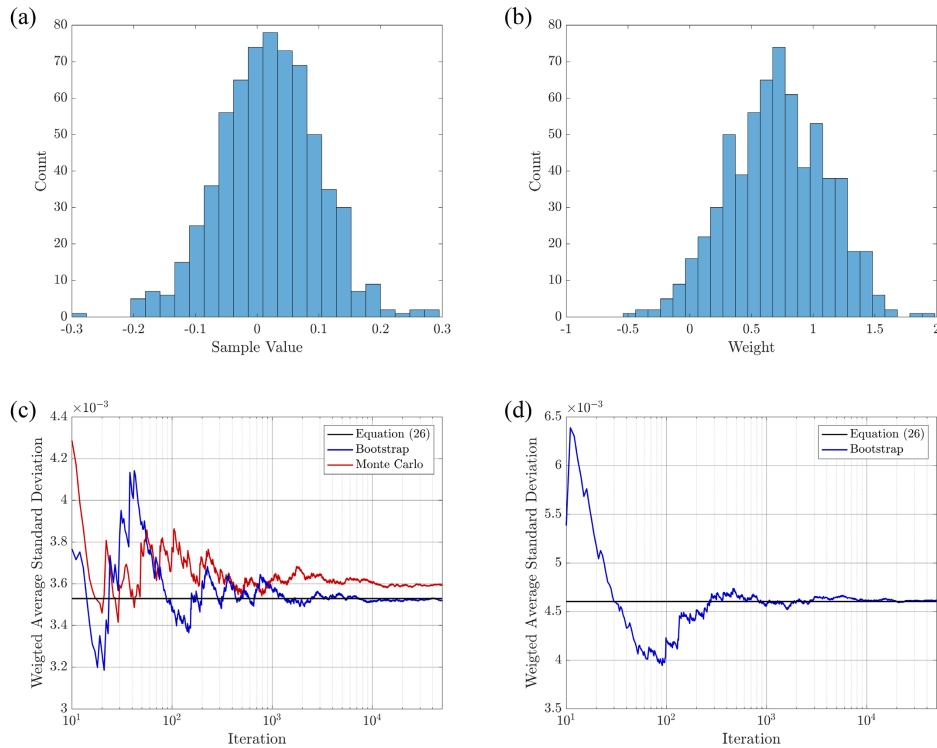
1117 **Figure 6.** Examples of converted phase delay time isochrons (curved surfaces) for Sp (a) and Ps
 1118 (b) phases. This case is for a half space with $V_p=7.8$ km/s and $V_s=4.3$ km/s. Conversion points
 1119 are at 200 km depth and ray paths are shown by red lines. The station is a blue triangle at (0 km,
 1120 0 km, 0 km). The black mesh at 200 km depth shows the horizontal plane for CCP stacking. (a)
 1121 The isochron for Sp scattering, with an incident S wave ray parameter of 0.1098 s/km. Delay
 1122 time for the isochron is -27.76 s. Colors on the isochron are the slope angle calculated from
 1123 equation (12). (b) Similar to (a) but for Ps scattering, and an incident P wave ray parameter of
 1124 0.0482 s/km. Delay time for the isochron is 21.74 s

1125



1126

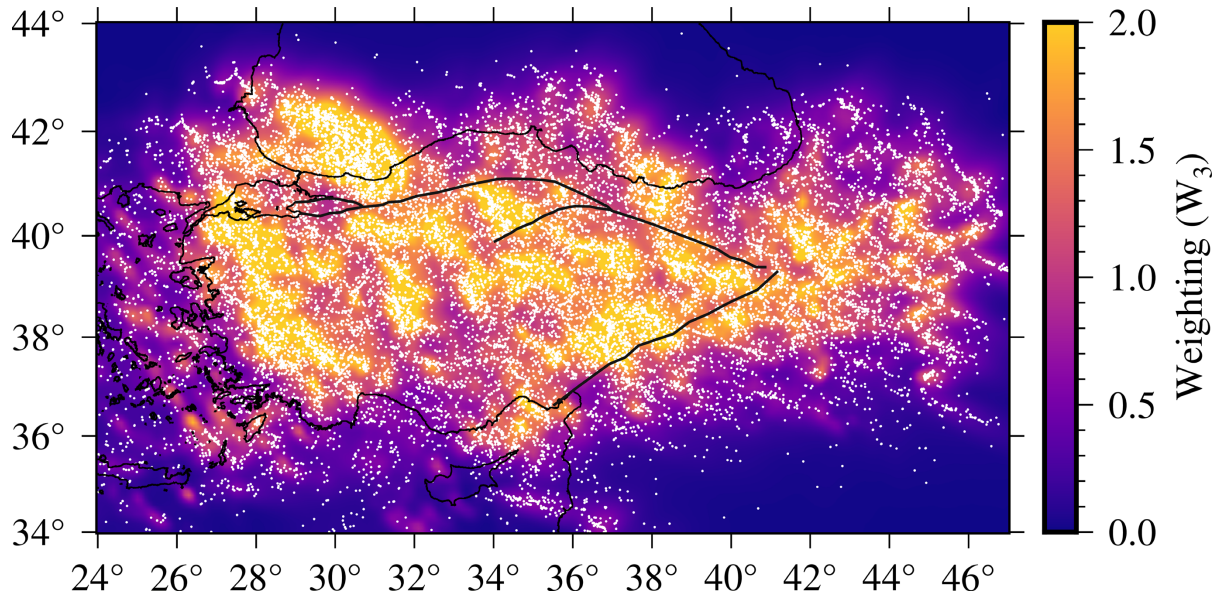
1127 **Figure 7.** Properties related to the weighting function in equation (16) calculated for the same
 1128 structure as used in Figure 6. (a)-(e) correspond to the Sp scattering case in Figure 6a and are for
 1129 a depth of 200 km. The red circle shows the conversion point, and the triangle shows the
 1130 horizontal position of the station projected downward from the surface. (a) The slope angle
 1131 distribution based on equation (12). (b) The geometric distance from each point to the station. (c)
 1132 The depth offset from the isochron to the stacking depth at 200 km (black mesh in Figure 6a). (d)
 1133 The depth offset estimated based equation (15) which is comparable to the true depth offset in (c)
 1134 near the conversion point. (e) The complete weighting function based on equation (16) that
 1135 combines information in (a), (b) and (d); (f) Similar to (e), but for the Ps scattering case in Figure
 1136 6b.



1137

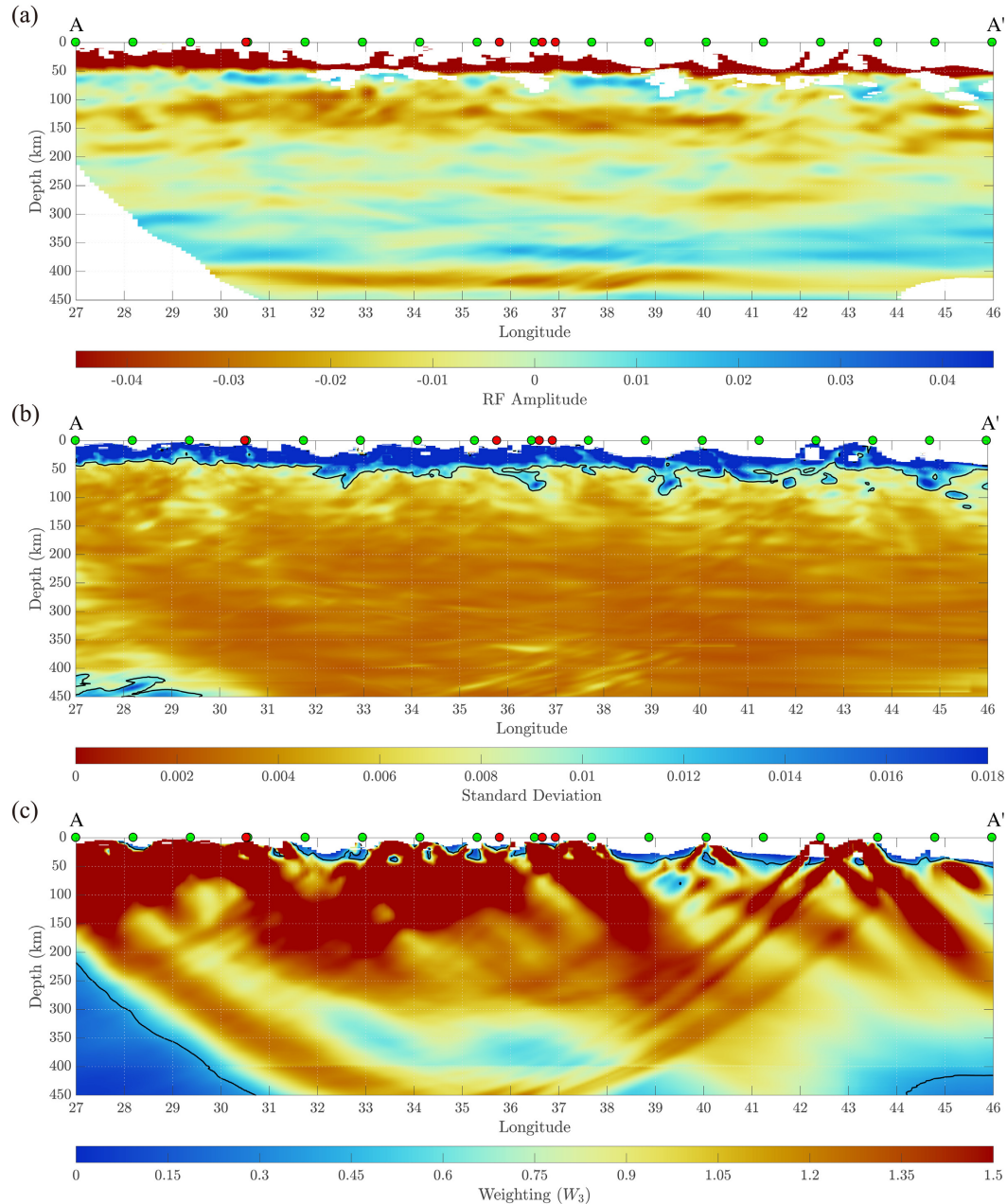
1138 **Figure 8.** (a) Histogram of 648 randomly generated samples from a normal distribution of
 1139 $N(0.02, 0.08^2)$, and the bin width is 0.024. (b) Histogram of 648 randomly generated weights
 1140 from a normal distribution of $N(0.7, 0.4^2)$, and the bin width is 0.101. (c) The standard deviation
 1141 of the weighted average of the samples in (a) with weights in (b). The black line shows the
 1142 standard deviation estimate from equation (26); the blue line shows the standard deviation
 1143 estimate from bootstrapping, where the x-axis shows the number of bootstrap iterations; the red
 1144 line shows the true standard deviation estimated from a Monte Carlo approach, where the x-axis
 1145 shows the number of Monte Carlo simulations. (d) The standard deviation of the CCP stack of
 1146 Anatolia receiver function amplitudes at 40.5°N , 38°E and 125 km depth; the lines have the same
 1147 meaning as in (c).

1148



1149

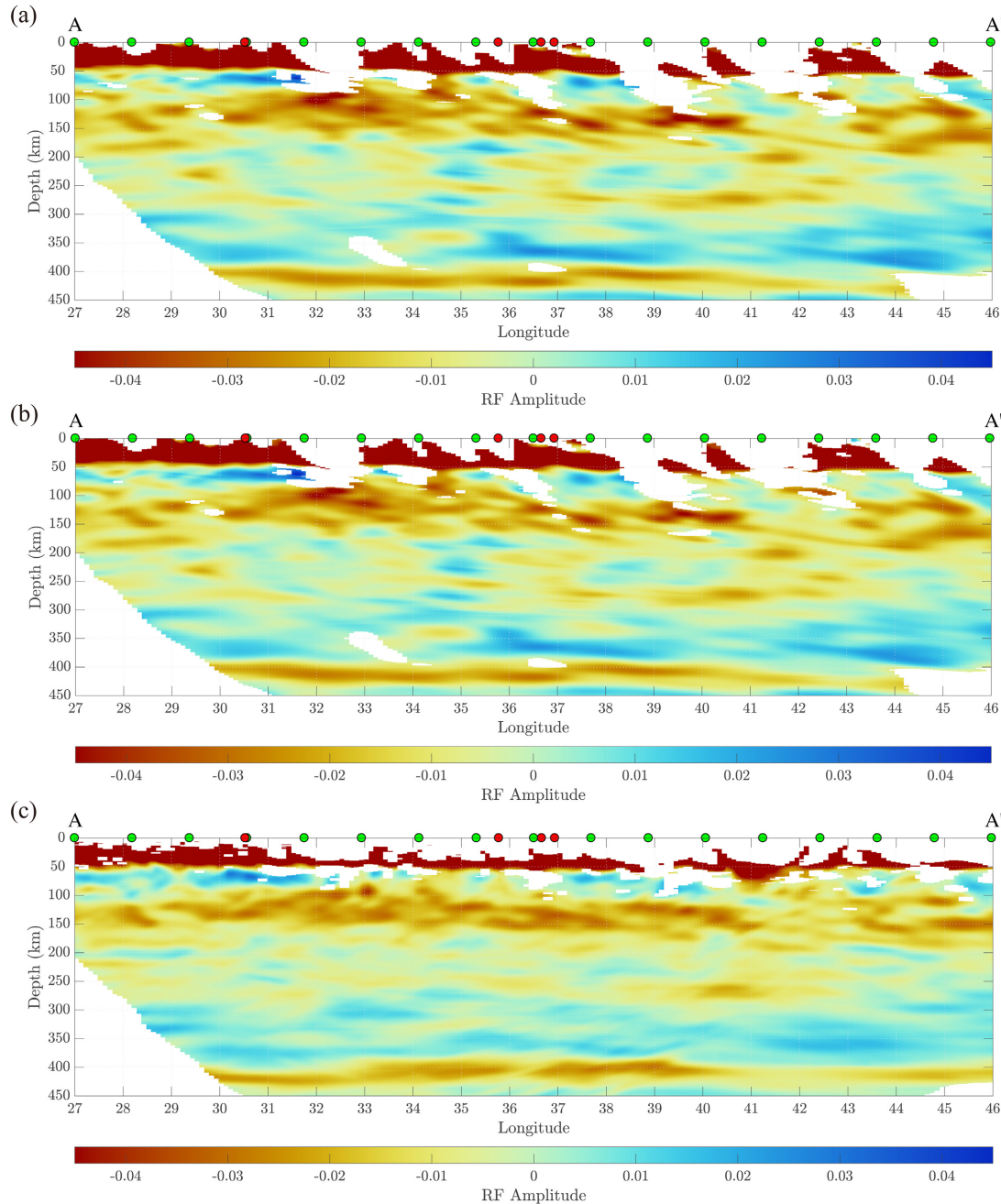
1150 **Figure 9.** Sp receiver function data sampling of the Anatolian region. Color shows the combined
1151 receiver function weights, W_3 (equation 27), at 125 km depth. Locations with W_3 values of more
1152 than 2.0 are shown by the yellow color that corresponds to 2.0 on the scale. White dots are
1153 piercing point locations of the 23,787 converted P wave ray paths. The weighting is generally
1154 stronger where piercing points are denser.



1155

1156 **Figure 10.** Properties of the Sp CCP stack shown on east-west oriented profile A-A' at 40.5°N.
 1157 Horizontal axes are annotated with longitude, and vertical axes are annotated with depth. The
 1158 location of the profile is shown in Figure 1. Green circles at the top of the profiles correspond to
 1159 green circles on the map, with 100 km distance between them. Red circles show the intersection
 1160 point of the profile with the North Anatolian Fault or East Anatolian Fault. The length of the
 1161 profile is 1,603 km. (a) Sp CCP stack amplitude. Red amplitudes correspond to negative Sp
 1162 phases and a velocity increase with depth (e.g. the Moho above 50 km and the 410-
 1163 discontinuity); blue amplitudes correspond to positive Sp phases and a velocity decrease with
 1164 depth. Phases with amplitude exceeding the limit of the color bar are shown by the boundary
 1165 color (e.g. the Moho phase). Blank areas indicate zones where the image is not robust and should
 1166 not be interpreted, either due to a standard deviation that exceeds both 0.01 and half of the

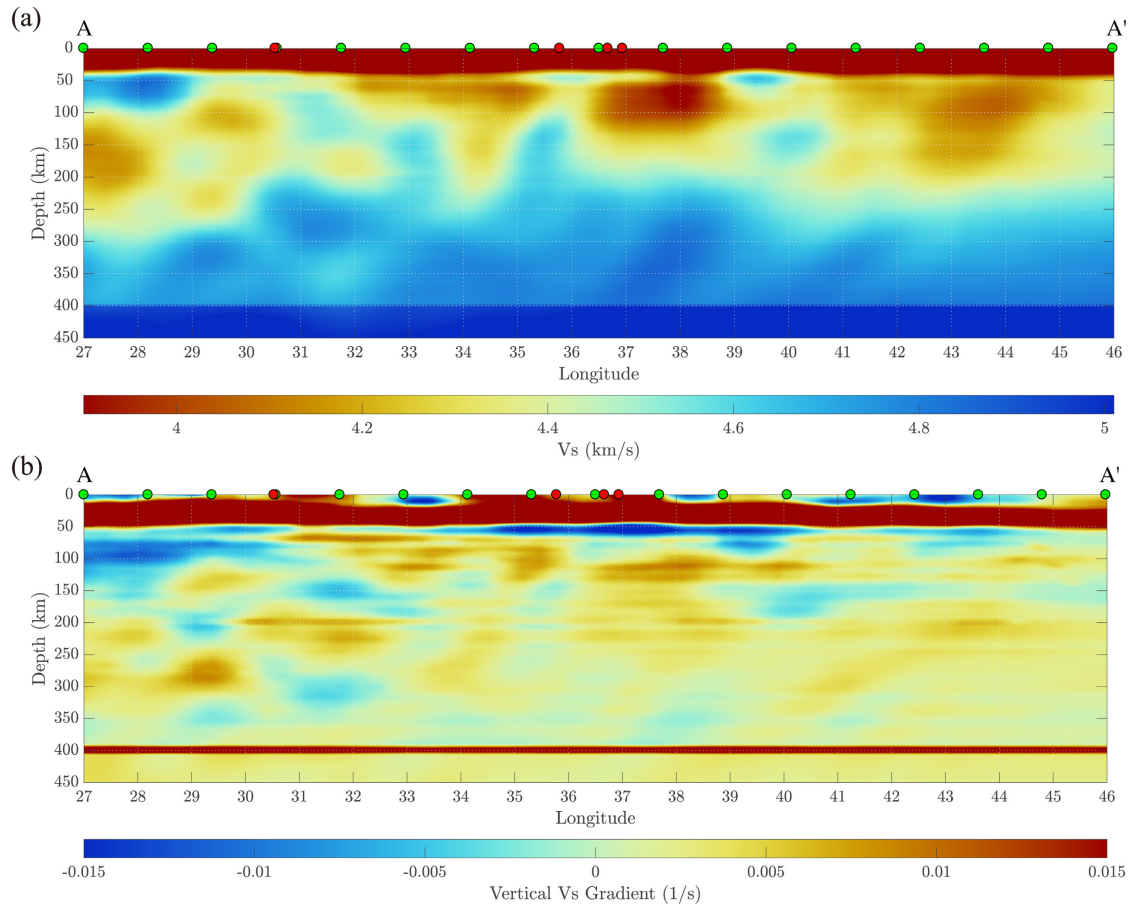
1167 receiver function amplitude, or due to a weight value W_3 (equation 27) that is less than 0.4. (b)
1168 The standard deviation of the Sp CCP stack amplitude from equation (26). Black line shows the
1169 contour where standard deviation equals 0.01. c) The total weight W_3 . Black line shows the
1170 contour where equals 0.4. Locations with W_3 that is more than the limit of the color bar are
1171 shown by the maximum color. The color map used in this figure and all others with CCP stacks
1172 is from Cramer (2018) although with a 50% increased saturation.
1173



1174

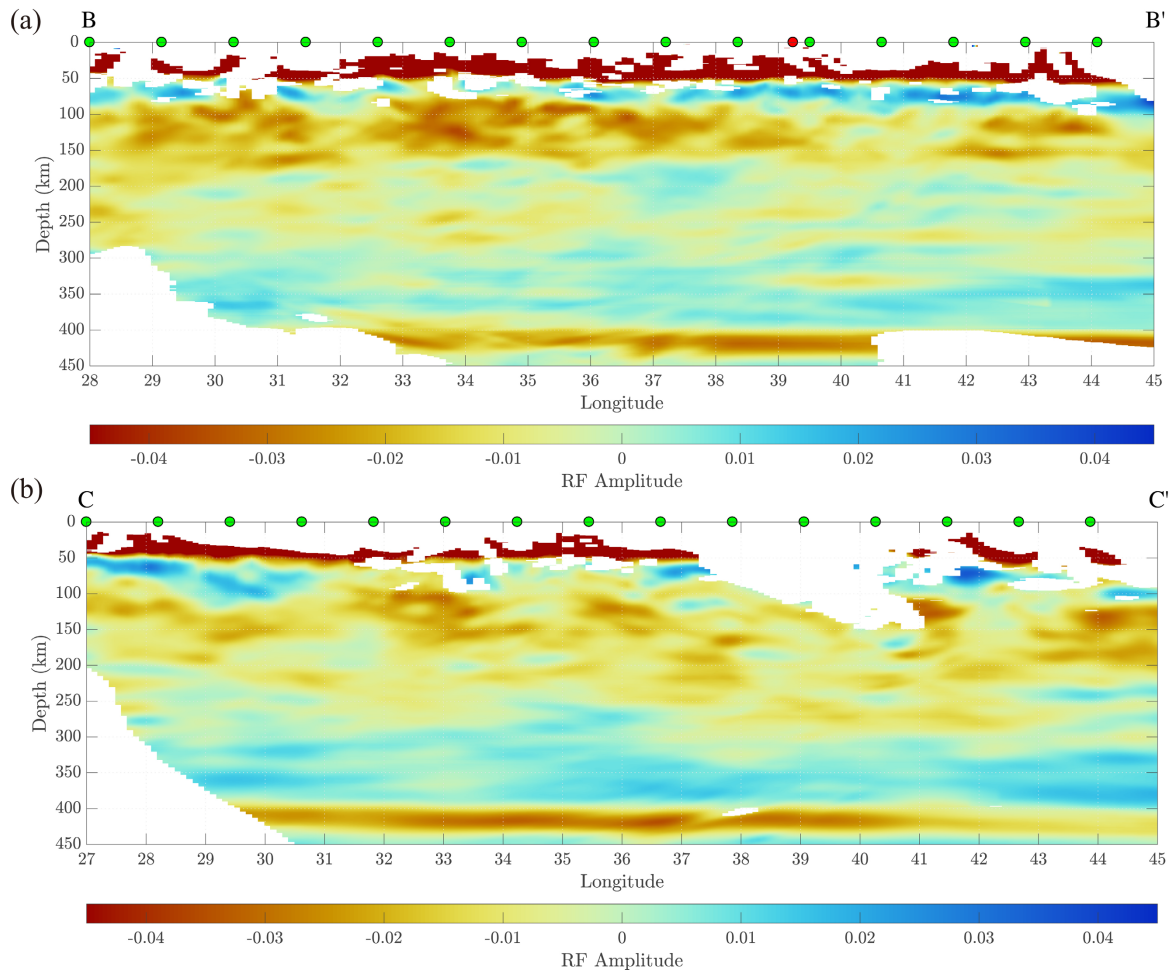
1175 **Figure 11.** Sp CCP stack amplitudes on profile A-A' using different methods and velocity
 1176 structures. Symbols and notations identical to Figure 10a. (a) CCP stack obtained using the
 1177 empirical weighting function defined by a 13 s P wave Fresnel Zone (Lekic et al., 2011).
 1178 Because the weighting function is defined differently than in Figure 10a, locations with W_3 less
 1179 than 40 are blank, while the criteria for standard deviation are the same. (b) CCP stack using the
 1180 free-surface velocity determination method in Abt et al. (2010), and the stacking method as in
 1181 (a). Blank regions are identified identically to (a). (c) CCP stack using the methods also used in
 1182 Figure 10a, except with the full-waveform inversion model of Fichtner et al. (2013). Blank
 1183 regions are identified identically to Figure 10a.

1184



1185

1186 **Figure 12.** Shear velocity model on profile A-A'. (a) Shear wave velocity from Blom et al.
 1187 (2020). Velocities exceeding the limit of the color bar are shown by the color at the limit (e.g.
 1188 crustal velocities). (b) Vertical gradients in shear-wave velocity from Blom et al. (2020)
 1189 smoothed over a 5 km depth window.



1190

1191 **Figure 13.** Sp CCP stack amplitudes on east-west profiles B-B' and C-C'. Symbols and
 1192 notations identical to Figure 10a. (a) Profile B-B' is located at 38.4°N, and the length of the
 1193 profile is 1,479 km. (b) Profile C-C' is located at 41.6°N, and the length of the profile is 1,494
 1194 km. Profile locations shown in Figure 1.

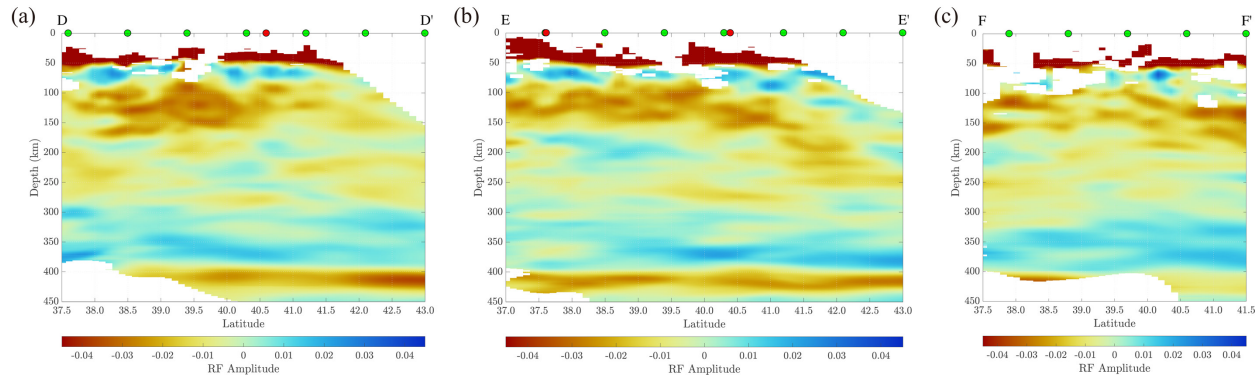
1195

1196

1197

1198

1199



1200

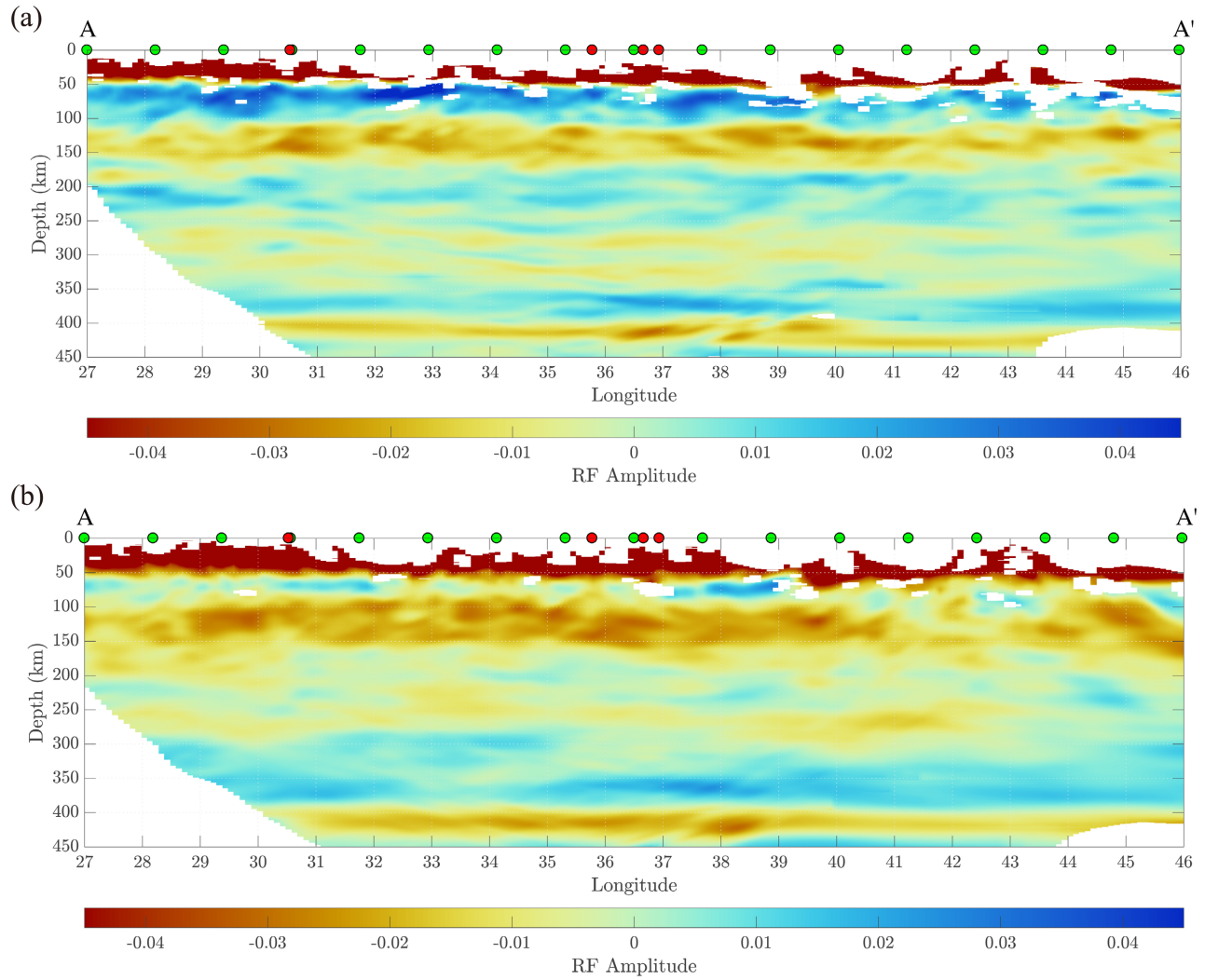
1201 **Figure 14.** Sp CCP stack amplitudes on north-south oriented profiles D-D', E-E' and F-F'.
 1202 Symbols and notations identical to Figure 10a, but horizontal axes are labeled with latitude. (a)
 1203 Profile D-D' is located at 31.18°E , and the length of the profile is 612 km. (b) Profile E-E' is
 1204 located at 37.35°E , and the length of the profile is 667 km. (c) Profile F-F' is located at 44°E ,
 1205 and the length of the profile is 445 km. Profile locations shown in Figure 1.

1206

1207

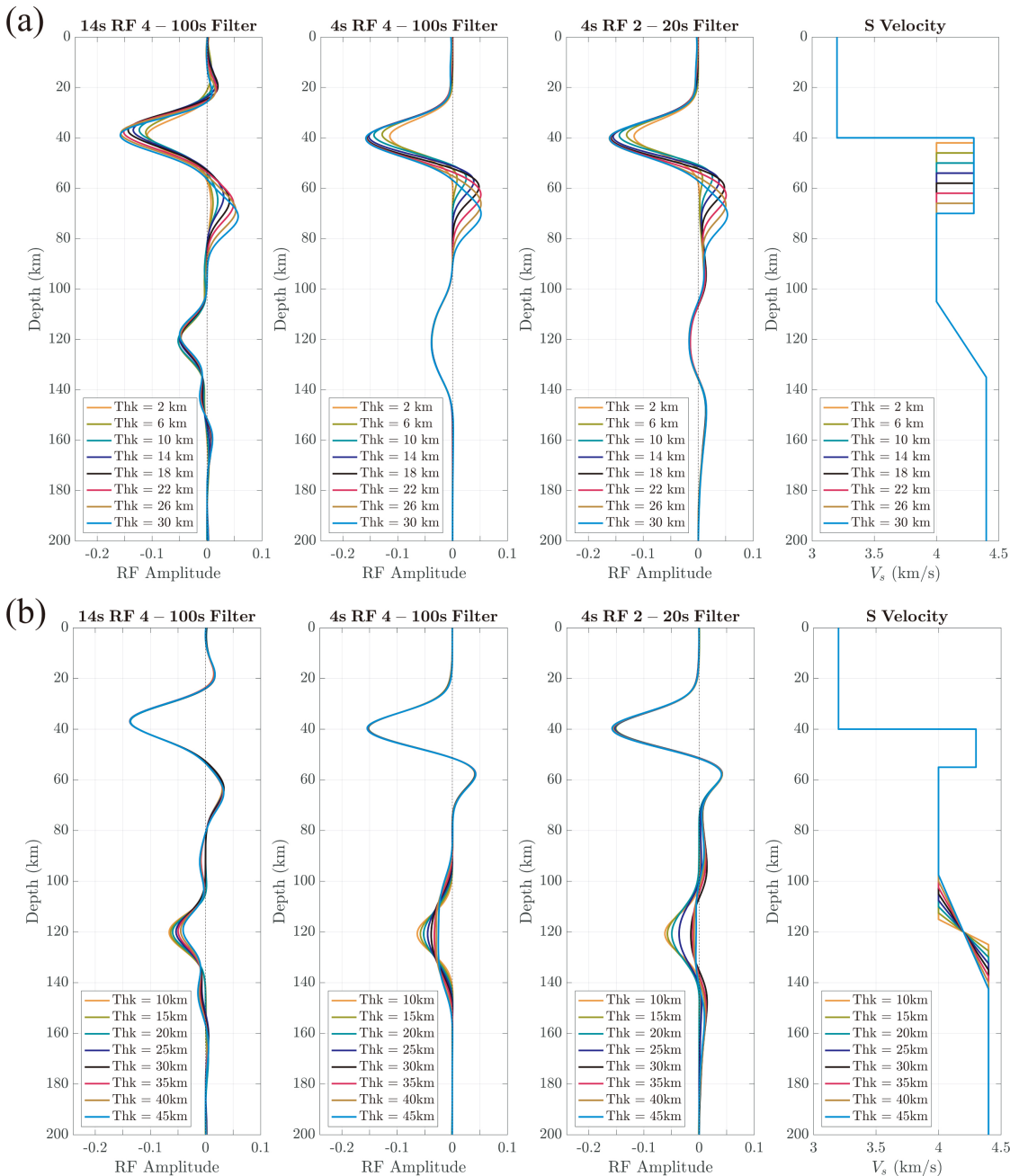
1208

1209



1210
 1211
 1212
 1213
 1214

Figure 15. (a) Similar to Figure 10a but using a 2 to 20 s bandpass filter before deconvolution. Clear LAB phases are observed around ~70 km depth. (b) Similar to Figure 10a but using a 10 to 100 s bandpass filter.



1215

1216 **Figure 16.** The frequency dependence of Sp receiver functions. (a) Synthetic Sp receiver
 1217 functions for velocity models with varying mantle lithosphere thickness from 2 km to 30 km as
 1218 indicated by the legend. The S waves have a ray parameter of 0.1098 s/km. Shear velocity
 1219 structures are shown in the right-most panel and the mantle lithosphere is characterized by a high
 1220 velocity layer starting from 40 km depth. The left-most panel shows receiver functions calculated
 1221 from synthetic seismograms whose source-time functions are characterized by Gaussian first
 1222 derivatives peaked at 14 s (~ 0.07 Hz). These waveforms were filtered with a 4 to 100 s bandpass
 1223 filter before deconvolution. The middle-left panel is similar to the left-most one, but with source-
 1224 time functions whose Gaussian first derivatives are peaked at 4 s (0.25 Hz). The middle-right

1225 panel is similar to the middle-left one, but with a 2 to 20 s bandpass filter. The LAB phase is
1226 larger amplitude for the cases where the source-time function has a 4 s period. (b) Sp receiver
1227 functions for structures where the positive velocity gradient at the base of the low velocity
1228 asthenosphere at 120 km has a varying depth extent. Velocity increases from 4.0 km/s to 4.4
1229 km/s within a layer as thin as 5 km to as broad as 45 km and, as indicated by the legend. The
1230 panels are arranged in the same way as in (a). Gradual positive velocity gradients (30-45 km
1231 depth extents) produce significant phases in seismograms with short-period (4 s) source-time
1232 function seismograms and the 4-100 s filter, but the amplitudes of these phases are reduced with
1233 the 2-20 s filter.

1234

1235

1236